Evaluating the quality of Controlled Meteorological Balloons in Arctic air mass transformation over the Nordic Seas

Sander Løklingholm

Master's Thesis in Meteorology

UNIVERSITY OF BERGEN
GEOPHYSICAL INSTITUTE

June 1, 2023

Acknowledgements

Abstract

In situ measurements from Controlled Meteorological (CMET) balloons are used to study Arctic air mass transformation in marine cold air outbreaks (mCAOs) over the Nordic Seas. 6 CMET balloons were launched from Ny-Ålesund on 24 March-5 April 2022 in association with the ISLAS 2022 field campaign. In the aftermath, the data from the CMET balloons were quality controlled, and calculations of height and wind data were carried out due to extensive GPS outages encountered by the balloons. Subsequently, the data from CMET flight 2 and flight 4 are analyzed using comparisons with radiosondes, a dropsonde and AROME-Arctic forecasts with different lead times. The results revealed good agreement between the CMET and AROME-Arctic forecasts. The largest difference was found for potential temperature and wind speed. Increased forecast accuracy with decreasing lead time was present for both flights, with the smallest accuracy change in flight 4 for humidity.

Moreover, two simulations with the Lagrangian particle dispersion model FLEXPART-AROME are analyzed in order to verify one of the CMET flights. Two different forecast initializations and release locations were used, and the weighted mean trajectories at three different altitudes surrounding the CMET balloon were investigated. A decreasing absolute horizontal transport deviation (AHTD) with height was found, and further analysis revealed that vertical wind shears were located at the locations of increased trajectory errors. This study displays a quantification of the performance of CMET balloons in a challenging Arctic environment, and the study shows that it is possible to retrieve useful information on mCAOs from CMET balloons.

Contents

1. Introduction

Marine cold air outbreaks (mCAOs) are one of the main contributors to air mass transformation in the Nordic seas region (Pithan et al., 2018). Transport of cold and dry Arctic air over the bordering warmer ocean currents in the Fram Strait west of the Svalbard archipelago results in rapid exchanges of heat and moisture between sea surface and the lower troposphere (Papritz and Spengler, 2017). Induced heat and moisture fluxes generate a deepening convective boundary layer that is accompanied by pronounced cloud modifications within the mCAO air mass (Brümmer et al., 1992). Subsequently, this could give rise to high impact weather, bringing heavy snow showers, and high wind speeds to the nearby region. This could affect vulnerable human infrastructure in the area, including among others transportation, fisheries, and search and rescue operations (Terpstra and Watanabe, 2020).

Until now, weather forecasting models have shown less degree of forecast performance in mCAOs (Abel et al., 2017). This is partly because mCAOs contain several physical processes on meso and micro scale that depend on precise model depiction (Kähnert et al., 2021). On the other hand, model errors also originate from limited data assimilation opportunities in the Arctic, due to the sparse network of observations (Müller et al., 2017a). The region is mostly ocean covered and thinly populated, which makes in situ observations difficult, leading to a more requirement on model precision and remote sensing for the quality of weather forecasts (Müller et al., 2017a). Therefore, there is a need for more observations in the Arctic to improve model representation of mCAOs (Papritz and Sodemann, 2018). Observations from field campaigns combining several academic fields is useful in order to understand how different processes interact in a coupled atmosphere-ocean-ice system, especially in light of climate change and sea ice break up (Vihma et al., 2014).

To address the shortcoming of limited observations, deployed Controlled Meteorological (CMET) balloons have been used. CMET balloons are remotely altitude controllable helium balloons carrying instruments that measure and transmit real time meteorological data. CMET balloons are developed by Paul Voss, and possess similar payload weight as traditional weather balloons, but have the unique ability to drift with the background wind (Voss et al., 2013). This makes CMET balloons able to fly for several days, and do consecutive profiling through lower parts of the atmosphere in remote areas (Hole et al., 2016).

CMET balloons have been tested previously in the Arctic region (Mentzoni, 2011; Voss et al., 2013; Roberts et al., 2016). However, in contrast to the previously mentioned studies, that were summertime campaigns, there has never to the author's knowledge been carried out CMET flights during winter time mCAOs, which presents additional challenges like increased risk of icing, and reduced power due to minimal daylight.

For this study, CMET data from the ISLAS 2022 field campaign will be assessed and analyzed. The CMET observations will be implemented together with data from other weather balloons, output from the operational weather forecast system AROME-Arctic, and an advanced particle dispersion model FLEXPART-AROME, which forms the base for this study. The following research questions will be considered:

- Is it possible to obtain useful atmospheric data from CMET balloons during mCAOs in a challenging Arctic winter environment, and what are the limitations and required criteria for CMET data to be trustworthy in such conditions?

- How reliable are the data provided by CMET balloons in retrieving valuable information on air mass transformation in mCAOs?

The work will be presented in the following chapters. First, a background in mCAOs and previous CMET work is introduced, before an explanation of the applied methods including post processing and calculations are given. The methods will be followed by a short chapter on the conducted CMET field work, before a more detailed analysis from two of the CMET flights is presented. The results are then discussed, followed by a summary and conclusion of the main findings.

2. Background

2.1 Marine Cold Air Outbreaks

Marine cold air outbreaks (mCAOs) are outflows of cold air and take place when cold air is moved into warmer marine regions (Papritz and Spengler, 2017; Kolstad, 2017). MCAOs are accompanied by several physical processes as the cold air and the relatively warm ocean interact. Transformation of air masses is related to the diabatic changes, which is a consequence of the uptake of heat and moisture originating from the sea surface, and the following cloud formation and the fall out of precipitation. (Papritz and Sodemann, 2018).

MCAOs in the Nordic Seas originate from larger scale meridional winds that generate advection of air masses from the Arctic, and tend to coincide with blocking anticyclones on mid latitudes (Pithan et al., 2018). Various climatological studies on mCAOs in the Nordic Seas region have been done. Papritz (2017) investigated mCAOs in the Irminger Sea and found three main synoptic patterns responsible for mCAOs. One of the patterns, which was characterized by a high pressure anomaly over Greenland, was also recognized by Dahlke et al. (2022) as one circulation pattern responsible for mCAOs in the Fram Strait, in addition to low pressure anomalies over the Barents Sea. According to Dahlke et al. (2022), mCAOs in the Fram Strait have shown a decreasing tendency during the last 40 years, except for March that has had an increase.

Although slightly different thresholds have been used to identify mCAOs, a common CAO index is defined by the difference in potential temperature between 850 hPa altitude and the surface skin temperature ($\theta_{SKT} - \theta_{850}$), introduced by Papritz et al. (2015). The difference is required to be positive for CAOs to exist. This definition was utilized by Papritz and Spengler (2017) in the study of the climatology of winter time CAOs by the means of calculation of kinematic trajectories from the ERA-Interim model (Fig. 2.1). Based on the magnitude of the difference in $\theta_{SKT} - \theta_{850}$, Papritz and Spengler (2017) categorized CAOs into different subgroups from weak to strong, and discovered that the strongest CAOs occur above the Fram Strait.

2.1.1 Air mass transformation in mCAOs

Air masses are exposed to diabatic changes during mCAOs. Hence, mCAO air masses are likely to become statically unstable, which consequently, can cause rapid transformations in the air masses characteristics. The exchange of energy between the ocean and atmosphere by turbulent heat fluxes, including turbulent sensible and latent heat can exceed 100 Wm^{-2}, sometimes even above 500 Wm^{-2} (Papritz and Spengler, 2017), which is significantly higher than the global average of 20 Wm^{-2} (Brümmer et al., 1992). This results in diabatic heating of the atmosphere, resulting in a cooling of the ocean surface. The production of dense waters in the Greenland and Iceland seas is found to be connected to heat loss from the turbulent heat fluxes during infrequent, but intense mCAOs (Papritz and Spengler, 2017). The amount of sensible heat that gets extracted from the ocean is to a great extent controlled by the difference in potential temperature between the air and the sea surface, implying that sensible heat make up for most of the atmosphere's heat uptake at the early stages of the mCAO (Papritz and Spengler, 2017;
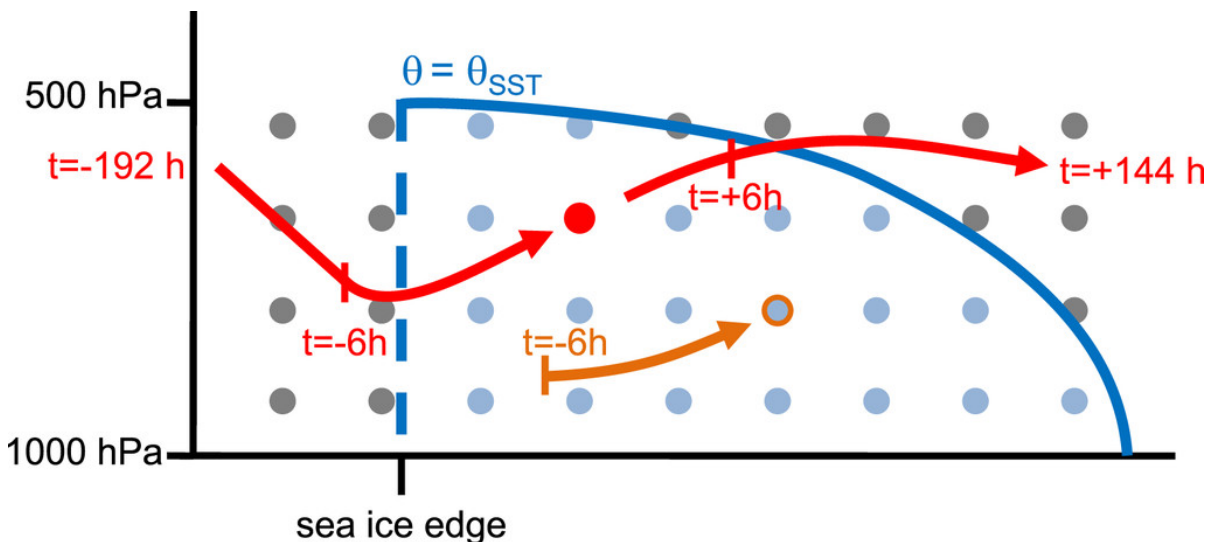
Papritz, 2017).

Figure 2.1: Schematic of a an air parcel's trajectory during a cold air outbreak. (Papritz and Spengler, 2017, Fig. 2).

In addition, sensible heat uptake is also to a great extent controlled by the wind speed (Papritz and Spengler, 2017). Wind speeds are according to Kolstad (2017) more intense than normal during the most intense mCAOs. The wind speed might also be enhanced near the sea ice edge due to development of an ice sea breeze circulation that overlaps the mean wind because of the strong thermally driven pressure gradients between ice and sea (Brümmer, 1996). The most abrupt changes in temperature and the strongest winds occur during periods with large CAO index values (Müller et al., 2017a). mCAO environments are also responsible for the formation of polar lows. Kolstad (2011) proposed an index for polar low occurrence, and found that the low level static stability restricts where polar lows can form, but that upper level forcing is the triggering factor.

2.1.2 Convective boundary layer

Central to the diabatic changes is the heat and moisture input. The fluxes destabilize the boundary layer and lead to vertical mixing. As a result, one gets the build up of a convective boundary layer that is characterized with an increasing boundary layer height. The boundary layer height marks the position of the inversion, distinguishing the boundary layer from the free troposphere above. Rapid boundary layer height modifications are not uncommon in mCAOs. Brümmer (1996) reported boundary layer heights changing from 100-300 m to 900-2200 m across a distance of 250 km during the ARKTIS 1993 field experiment outside Svalbard in March 1993.

Near the boundary layer top, stratocumulus clouds form. Initially, the Arctic air could be cloud free at low levels. Gradually, rolls of stratocumulus clouds appear due to condensation near the boundary layer top, that can be observed as cloud streets on satellite images following the mean wind direction, and are characteristic for mCAOs. The formation of these boundary layer roll vortices is explained by a combination of dynamic and convective instability, as well as different scales of motion acting together through nonlinear interactions (Etling and Brown, 1993).

The stratocumulus clouds then break up into convective cell structures. This transition

in cloud regime was extensively studied in Abel et al. (2017). They argued that the transition is controlled by precipitation and ice phase processes. When enough water vapor has evaporated and the air becomes saturated to become depleted, then the precipitation breaks the moisture source uptake for the stratocumulus clouds. This leads to a decoupling of the boundary layer and sets the stage for a change in cloud properties, favoring higher clouds that are more fed by the heat in association with latent heat release from the precipitation.

Further downstream the latent heat fluxes become more important. Enhanced sea surface temperatures lead to higher moisture fluxes. Papritz and Sodemann (2018) found that the mCAO air masses create their own water cycle, presenting a turnover time for the water that is roughly one day. This is significantly shorter than the global mean that lies within 8 to 10 days. In addition, the different pathways where the moisture is distributed are equal.

Challenges in the performance of numerical weather prediction models with regard to mCAOs are widely acknowledged. These can originate from different sources. Among others, false representation of sea ice because of drift or breakup could have an effect on the model's performance during mCAOs (Müller et al., 2017a). The timing of the break up in cloud morphology is still uncertain. Findings from Abel et al. (2017) suggest that that ice is currently too active in removing liquid, and consequently causing a too rapid cloud break up. Abel et al. (2017) also suggested that improvements in the microphysics schemes should be considered, as the representation of clouds also play a vital role with regard to radiative effects. There has also been an increased focus on the Lagrangian perspective of physical air mass transformation of mCAOs using Lagrangian modeling (Papritz and Spengler, 2017; Papritz, 2017). Nevertheless, pursuant to Pithan et al. (2018), there is a need for more novel observations of advecting air masses, which in order to obtain a greater understanding of the physical transformation processes in mCAOs.

2.2   Previous CMET work

Previous field campaigns that have targeted mCAOs in the Nordic seas have mostly been based on radiosonde or aircraft measurements. CMET balloons present the opportunity for Lagrangian measurements of upper air and boundary layer structures over a large region and can sustain longer flights compared to the other airborne measurements. CMET balloons have been tested and used for atmospheric research on several field campaigns (Roberts et al., 2016; Stenmark et al., 2014; Dale et al., 2020; Riddle et al., 2006; Mentzoni, 2011).

Five CMET balloons were launched from Ny-Ålesund on Svalbard in May 2011. Two of the flights were analyzed in Roberts et al. (2016) who compared CMET observations to the global ERA-Interim reanalysis product from ECMWF and the higher resolution Arctic system Reanalysis (ASR). The CMET balloons carried out multiple soundings of the atmospheric boundary layer above the sea ice east of Svalbard and along the ice free northwestern coastline. They found that the observed temperature and humidity were well simulated by both models, while ASR, was more able to reproduce inversions and wind shears. Roberts et al. (2016) also concluded that the CMET balloons were able to detect local scale wind fields during the two case studies.

CMET balloons have also been used for studying boundary layer structures in Antarctica. Stenmark et al. (2014) for instance, applied observations from CMET balloons launched from Dronning Maud land in January 2012 to study the impact of bare ground nunataks on free convection, and Dale et al. (2020) investigated observations from a CMET balloon campaign near the Ross sea polynomia in November 2017.

Due to the CMET balloon's relatively long spatio-temporal range, the balloons have been used in evaluation of different atmospheric transport models. Riddle et al. (2006) evaluated the trajectory model FLEXTRA with 5 CMET balloons deployed from the east coast of the US during July and August in 2004 as part of the International Consortium for Atmospheric Research on Transport and Transformations (ICARTT)-campaign. Riddle et al. (2006) evaluated the performance by calculating trajectorry errors between the CMET balloons and trajectories from FLEXTRA that were run on wind fields from ECMWF and GFS. It was found that using higher resolution input data did not necessarily improve the trajectory errors. Using a $1°$ ECMWF wind field and $1°$ GFS resulted in average relative trajectory errors of 26% and 34% respectively. However, Riddle et al. (2006) did report high variations in trajectory errors both between flights and during single flights, and therefore, suggested that a higher effort should be put into understanding the uncertainties that come with such model trajectories, especially in relation to subgrid scale effects.

Similar approach as in Riddle et al. (2006) was used by Mentzoni (2011), who evaluated FLEXTRA's successor FLEXPART together with 5 CMET balloons launched on Svalbard in August 2010. FLEXPART simulates Lagrangian particle dispersion, and was for this study initialized with input from the ECMWF $0.3°$ model. 50 imaginary air parcels were released from 5 different altitudes surrounding the CMET balloon's operating height. Despite a slightly higher resolution input data compared to Riddle et al. (2006), Mentzoni (2011) reported a similar average relative trajectory error of 28%.

An analogous approach to the preceding mentioned studies with verification of CMET to a numerical weather prediction model and trajectory model has been applied in this study. However, CMET balloons have not yet been used to study strong air mass transformation in mCAOs.

7

3. Methods

To study the development of mCAO air masses, observations from Controllable Meteorological (CMET) balloons launched during the ISLAS 2022 campaign will be used. The observations are post-processed and analyzed together with the weather forecasting model AROME-Arctic and the Lagrangian particle dispersion model FLEXPART. In the following chapter, a review of the CMET balloons, the applied processing measures, and the model setup is presented.

3.1   CMET Balloons

CMET balloons are vertically controllable helium balloons constructed to fly over several days and to cover large distances (Roberts et al., 2016). The balloons are supplied with a payload that accommodates instruments to measure and transmit air temperature, pressure, relative humidity and position. Data gets transmitted in near real time with the use of an iridium satellite modem. This feature enables the operator to monitor and regulate the balloon during the course of the flight.

3.1.1   Design and Characteristics

Every CMET balloon consists of an inner super pressure balloon and one outer balloon (Voss et al., 2013). The two balloon bladders are connected by a small pump and valve system, as indicated by the CMET schematic in Fig. 3.1. Together with an Iridium 9603 satellite modem (Iridium, US), the operator can adjust the buoyancy of the balloon by sending commands to the helium pump onboard via the balloon's control board. Releasing helium from the super pressure balloon will increase the buoyancy, causing the balloon to ascend, while pumping helium back will decrease the buoyancy, causing the balloon to descend. One can therefore control the altitude of the balloon on demand. The balloons are designed to reach an altitude of 3500 m. The typical vertical velocity is in the range of 0.5-1.5 ms^{-1}. This ability makes the CMET balloons able to carry out vertical profile measurements along the flight track.
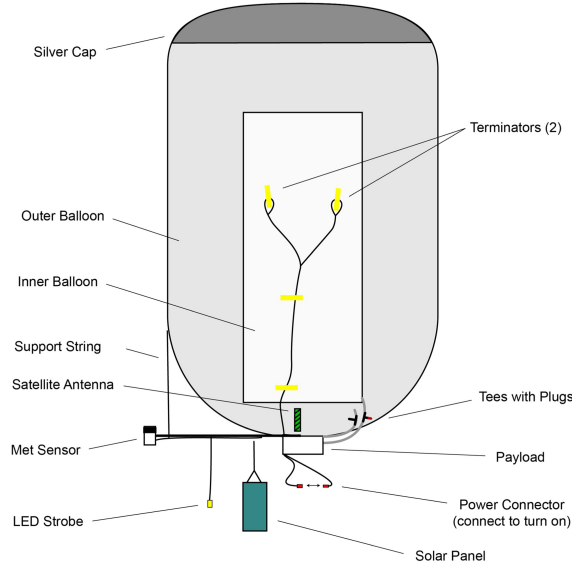
Figure 3.1: Schematic of the CMET balloon and the instrumentation (Dale et al., 2020, Fig. 1).

3.1.2 Instruments

The CMET balloon contains several types of instrumentation. The payload weighs approximately 230 g. In addition to the control board, the payload also features GPS, battery and solar panel. Position is measured by the Inventek ISM420 GPS receiver (Inventek, US), which has an accuracy of ± 10 m. The control board is powered by a lithium battery. In addition, some balloons are provided with a solar panel that can recharge batteries in favor of longer flights. An insulated pouch ensures payload temperature is kept at an adequate level for optimal operation, usually at +20 K above the ambient temperature (Dale et al., 2020). Data acquisition, sample rate and transmission rate varies from 10 s to 20 min, and 5 min to 1 h respectively. The sample and transmission frequency could be modified during the flight. High transmission rates can produce heat in order to maintain payload temperature, but can also be reduced in exchange for battery saving.

Atmospheric pressure is measured by the Freescale MPXH6115A (NXP Semiconductors, Netherlands) sensor. This is an aviation approved pressure sensor. Air temperature is measured by the MC65F103A (Amphenol, US) temperature sensor in Kelvin, in the range of -40 to 105 °C with an accuracy of 0.05 K. A SHT-35 (Sensirion, Switzerland) is used for measuring relative humidity, operating with an accuracy of 1.5% in the range of 0-100%. Full description of relevant instruments are shown in Table 3.1, and a photo showing the CMET balloons in action (Fig. 3.2). The meteorological sensors are attached to a 800 mm boom protruding horizontally out from the payload to avoid influence from the boundary layer surrounding the sensors (Dale et al., 2020).

Table 3.1: Instrumentation for meteorological and positional measurements. The columns show parameter, type, range and accuracy.

Parameter	Type	Range	Accuracy
Air temperature	MC65F103A	-40-105 °C	0.05 K
Relative Humidity	SHT-35	0 - 100% RH	1.5%
Atmospheric pressure	Freescale MPXH6115A	15-115 kPa	1.5 % (0-85°C)
Lon/Lat/Alt	Inventek ISM420	0-18,000 m	10 m
Lon/Lat	Iridium 9603	Global coverage	Unknown

A variety of technical adjustments were made in order to retrieve as much data as possible for the scientific objectives of the ISLAS2022 campaign. The total weight was reduced from 250 to 230 g. Together with firmware and operational changes, the battery weight was reduced to optimize flying time. In addition, an aspiration fan was discharged to remove a warm bias that had caused issues during previous CMET flights. In order to gain better control, the super pressure balloon, however, was made 10% larger.

Figure 3.2: CMET balloons during flight 5 and flight 6 right after the night time dual launch in Ny-Ålesund on 4. April 2022. Photo: Lars Robert Hole.

3.2 ISLAS 2022 Campaign

In total 6 CMET balloons were deployed during the Isotopic Links to Atmospheric water's Sources (ISLAS) 2022 campaign. ISLAS2022 was an intensive field campaign that was conducted in the period March-April 2022, and involved different institutions, led by Prof. Harald Sodemann, and coordinated across several sites in the Nordic Sea region, with Kiruna in northern Sweden as a main site. The campaign was part of the ISLAS research project, funded by the European Research Council. The overall aim of ISLAS is to understand the water cycle by studying isotopic composition, from evaporation to precipitation. Due to the ideal conditions mCAOs represent for this purpose, the campaign targeted mCAOs.

Together with a research aircraft stationed at Kiruna Airport, and a research vessel situated in the Norwegian Sea, the CMET balloons role was to collect in situ measurements

during mCAOs. Specifically, the launching of CMET balloons had two main intents. 1) Follow the physical transformation of an Arctic originated air mass as it entered the Nordic Seas from the west of Svalbard. 2) Provide data for evaluation of the Lagrangian particle dispersion model FLEXPART (Pisso et al., 2019).
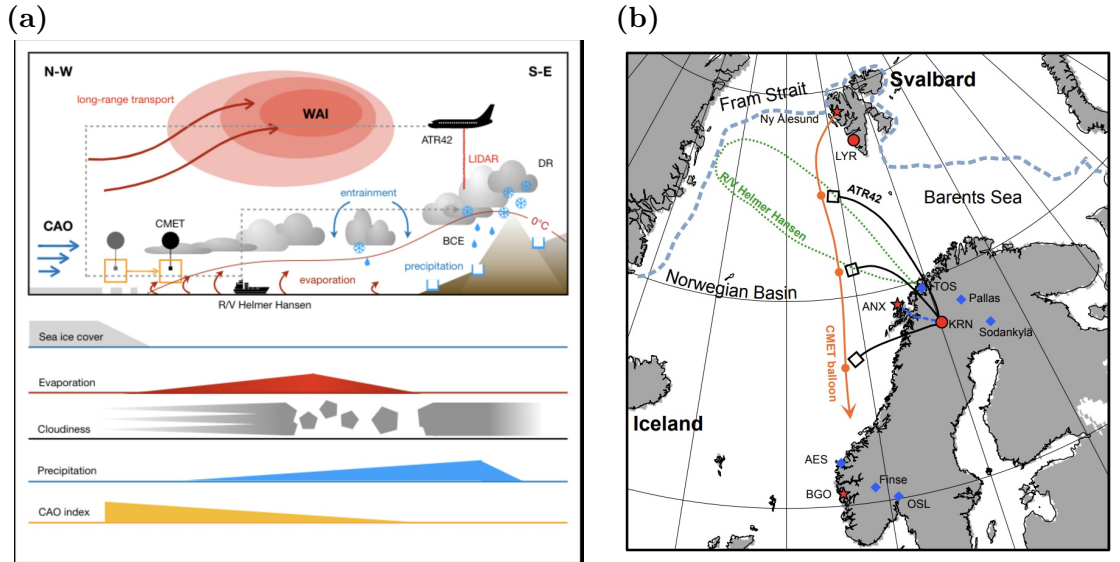
(a)   **(b)**

Figure 3.3: ISLAS campaign implementation plan with a cross section schematic showing the mCAO framework (a), and map of the main locations and expected CMET balloon trajectory (b) (Sodemann, 2022).

3.3 Data Processing

Data from the CMET balloons has been processed in terms of different aspects such as altitude and coordinates. The data from the acquisition system was automatically collected and stored in a raw data set. In addition to the atmospheric variables, different control parameters such as payload temperature, pump duty, battery power and command counts were stored in the raw data set as well (Voss et al., 2013). Different relevant variables were then retrieved from the raw data set in order to create a new enhanced quality controlled data set. The retrieved variables were used to calculate potential temperature, virtual temperature, specific humidity and mixing ratio to restore missing data as detailed below.

3.3.1 GPS Correction

GPS position information during the CMET flights encountered issues. Due to unpredictable dropouts of GPS signals, information on both coordinates and altitude is inaccurate at specific periods on most CMET flights. Some flights were affected throughout the entirety of the flight, while others had limited signal dropout (Appendix B, Figs. B.1 a-f).

Gap filling

Both Iridium and GPS have been used to obtain coordinate data. The approximate position of the CMET's longitude and latitude is retrieved every time there is a transmission going through the Iridium satellite modem. Iridium coordinates have therefore

been extracted from every data transmission to fill in missing GPS coordinates. However, the number of retrieved Iridium coordinates is lower compared to the number of GPS points, and the Iridium position is consequently more uncertain. In order to merge high resolution GPS with lower resolution Iridium data a linear interpolation formula has been used, as shown in Eq. 3.1 (Thomson and Emery, 2014).

$$y(x) = y(a) + \frac{x - a}{b - a}[y(b) - y(a)] \tag{3.1}$$

Here, the two known coordinate points (a, y(a)) and (b, y(b)) are used to find the y(x) value on a straight line between the two known coordinate positions.

3.3.2   Wind calculation

Wind data was only stored in the raw data set when the GPS signal was stable. Consequently, the lack of GPS signal led to a lack of wind data in the raw data set. Broadly estimated wind data has therefore been calculated. The functions for deriving the horizontal wind components (Eq. 3.2, 3.3) are adapted from the wind estimation formula used for estimating wind from GPS coordinates in the raw data set. These give the balloon's horizontal velocities based on the change in latitude and longitude with respect to time. u_g and v_g are derived in the following way,

$$u_g = cos\left(y\frac{\pi}{180}\right) r\Delta x \left(\frac{\frac{\pi}{180}}{\Delta t}\right) \tag{3.2}$$

$$v_g = r\Delta y \left(\frac{\frac{\pi}{180}}{\Delta t}\right) \tag{3.3}$$

where x, y and r denote longitude, latitude and Earth radius, respectively. Δx and Δy are the changes in longitude and latitude for every time step Δt. The two components are then combined to find the total wind speed W_s and direction W_d (Eq. 3.4, 3.5).

$$Ws = \sqrt{u_g^2 + v_g^2} \tag{3.4}$$

$$Wd = \tan^{-1}\left(-\frac{u_g}{v_g}\right) \cdot \frac{180}{\pi} \tag{3.5}$$

Due to occasionally unrealistically high wind speeds from this method, a maximum wind speed threshold was used (Table 3.2). For the CMET flight with the highest recorded wind speed, the maximum wind speed was found to be more than 3 standard deviations away from the mean wind speed. It was therefore considered that the maximum recorded wind speed for the CMET flights could be used as a sufficient upper threshold for the wind calculation. However, if the CMET flight did not have any GPS signal at all, such as during flight 4 (Table 3.2), the maximum wind speed out of all the other CMET flights was used as an upper threshold, in this case 24 ms^{-1}. The cut of values have been filled with neighboring values followed by a forward moving average time series filter of 10 consecutive data points. The full summary of applied threshold and mean wind speeds

for the CMET flights is shown in Table 3.2. Note that the mean here is based on the raw data, and does not account for the new calculated wind speeds. The calculated wind data is used to fill the missing wind data gaps.

Table 3.2: Applied wind speed thresholds for the wind speed calculation and the mean wind speeds from the raw data set for CMET flight 1-6.

Flight no.	Threshold (ms^{-1})	Mean (ms^{-1})
1	12.9	4.95
2	24.0	10.10
3	10.5	3.98
4	24.0	No data
5	11.3	5.36
6	19.8	2.50

3.3.3 Height calculation

To deal with missing GPS height information, a pressure derived altitude was calculated. A pressure derived altitude variable was already included in the raw data set. However, since it uses the US Standard Atmosphere, and was showing offsets with the GPS altitude, the existing altitude was rejected in favor of a modified pressure derived altitude based on the hypsometric equation. The following way to proceed is adapted from Wallace and Hobbs (2006), which states the following,

$$T_v = T(1 + 0.608w) \tag{3.6}$$

The virtual temperature T_v is then estimated from temperature T and mixing ratio w from the closest radiosonde launch in Ny-Ålesund. Profiles that are used for altitude approximation are shown in Appendix A, Table. A.1. By applying Eq. 3.7 from Wallace and Hobbs (2006), a mean virtual temperature can be computed:

$$\overline{T_v} = \frac{\int_{p_2}^{p_1} T_v \, d(lnp)}{\int_{p_2}^{p_1} d(lnp)} \tag{3.7}$$

Eq. 3.7 is simplified to Eq. 3.8, and applied to in total five layers with heights of 100 hPa in the range between 1000-500 hPa. This gives five $\overline{T_v}$ values, which are scaled with their respective pressure differences.

$$\overline{T_v} = \frac{\int_{p_2}^{p_1} T_v \left(\frac{dp}{p}\right)}{ln\frac{p_1}{p_2}} \tag{3.8}$$

Substituting $\overline{T_v}$ into Eq. 3.9 and including the constant for dry air $R_d = 287$ JK^{-1}kg^{-1}, and the gravitational acceleration constant $g_0 = 9.8$ ms^{-2}, we can get an approximation of the scale height $\overline{H}$.

$$\overline{H} = \frac{R_d \overline{T_v}}{g_0} \tag{3.9}$$

The $\overline{H}$ is then used to compute altitude. Applying pressure data from the CMET in Pa where two consecutive values are represented as p_1 and p_2, and setting Z_1 equal to the height of the launch site, $Z_1 = 17.4$ m, leaves us with an equation with one unknown, Z_2. By rearranging terms, we can estimate Z_2 for every single pressure difference, shown in Eq. 3.10. Adding all the calculated altitudes for Z_2 to Z_1, a more sophisticated altitude parameter can be approximated.

$$Z_2 = \overline{H}ln\frac{p_1}{p_2} + Z_1 \tag{3.10}$$

3.3.4 Quality Flags

Because of factors such as irregular GPS signal, variable sampling resolution, and reliability of the sensors in the cold Arctic environment, I chose to assign quality flags to allow for filtering of the data during analysis. 4 quality flags have been computed and assigned to the measurement data in a netcdf file format. The filtered data will be regarded in more details in the results and discussion chapters.

The quality flags are based on 5 tests that have been applied on the data set (Table 3.3). The tests are chosen by the author, and include checking raw CMET data with regard to possibility of 1) vertical velocity, 2) coordinates, 3) signal frequency, 4) sampling frequency, and 5) measurement errors.

First, a test that evaluates the balloon's vertical velocity was defined. The absolute value of the vertical velocity can be approximated by the balloon's ascend and descend rate, which is found from the vertical distance covered by the balloon per time step. Test 1 is predicated on the assumption that the removal of the balloon's fan might artificially enhance the temperature measurements in a low wind speed environment. Therefore, a limit of $\pm\ 0.2$ ms^{-1} vertical speed was introduced to indicate that observations are taken when the sensors experience sufficient ventilation.

In test 2, a procedure was constructed to pinpoint uncertain position information. If a missing GPS signal is encountered, the lack of coordinates are filled with iridium coordinates. However, when either GPS or iridium coordinates are not accounted for, test 2 fails. This implies that position information is represented by interpolated coordinates, which carry an increased amount of uncertainty.

Data during low temporal resolution could suffer from an unrealistic high rate of change in the parameters. The phase of flight could induce sporadic variations during ascending or descending stages. Hence, to ensure reasonable data, two time gaps tests were implemented to check temporal resolution, test 3 and 4. Test 3 flags position data that are retrieved after a 30 min time gap. Consequences could be that interpolation of position data becomes more challenging with higher time gaps. Test 4 checks sampling resolution of the meteorological parameters, and flags the data that are retrieved after a 15 min time gap.

Last, in order to detect potential outliers, the time rate of change of the retrieved parameters have been treated in test 5. Threshold values for the time derivative of temperature, relative humidity and pressure were set to 10 K, 100% and 10 hPa per minute respectively. In addition, a filter for flagging out relative humidity data surpassing 100% was activated.

Table 3.3: Description of the quality tests and its associated threshold criteria and implications.

Test no.	Description	Threshold criteria	Implications
1	Vertical velocity	$|w| < 0.2 \text{ ms}^{-1}$	Unrealistic data possible
2	Both GPS and iridium signal	Missing $\vec{x_{GPS}}$ and $\vec{x_{iri}}$	Interpolated data
3	Signal frequency	t > 30 min	Time gaps
4	Meteorological sensors sampling frequency	t > 15 min	Time gaps
5	Measurement error	$\frac{\Delta T}{\Delta t} > 10 \text{ K min}^{-1}$ $\frac{\Delta RH}{\Delta t} > 100\% \text{ min}^{-1}$ $\frac{\Delta hPa}{\Delta t} > 10 \text{ hPa min}^{-1}$ RH > 100 %	Unrealistic data

Based on the outcome of the tests above, the data are flagged with a number from 0 to 3, and are shown in Table 3.4. Good data acquires flag no. 0, meaning data passed all tests. If one or more tests fail, the data are assigned with a number from 1 to 3 determined by the number of tests the data fail to fulfill. Dubious data and probably poor data are enumerated by number 1 and 2 correspondingly. In case that three or more tests fail, however, the data are classified as poor quality, with flag no. 3.

Table 3.4: Quality flags. A ranking from 0-3 based on the amount of tests that are satisfied.

Flag no.	Quality	Meaning
0	Good data	All tests passed
1	Dubious data	1 test failed
2	Probably poor data	2 tests failed
3	Poor data	3 or more tests failed

3.4 Final data set variables

The final data set variables are shown below (Tab. 3.5). After the quality checking, the retrieved parameters were stored in a final data set that has been used for the analysis. Both GPS altitude from the raw data set and the calculated altitude are included, in addition to longitude and altitude data. There are also data variables that have been directly converted from the raw data set, such as air temperature, relative humidity and air pressure. The remaining variables are the calculated air potential temperature, virtual temperature, mixing ratio, wind speed and wind direction.

Table 3.5: The final data set variables with correponding units

Retrieved parameters	Unit
GPS Altitude	m
Altitude	m
Latitude	°N
Longitude	°E
Air temperature	K
Air potential temperature	K
Virtual temperature	K
Relative humidity	%
Specific humidity	gkg^{-1}
Mixing ratio	gkg^{-1}
Air pressure	hPa
Wind speed	ms^{-1}
Wind direction	°

3.5   Radiosonde and dropsonde data

Radiosonde and dropsonde data have been utilized in comparison with the CMET data. Radiosondes provide good estimates of the vertical profile of the atmosphere. In the Norwegian Arctic, radiosondes are regularly launched from the meteorological station on Bjørnøya and from the supersite in Ny-Ålesund. Data from a profile provided by a HALO dropsonde was also used. The High Altitude and Long Range Research Aircraft (HALO) is a German research aircraft that participated in the international HALO-(AC)[3] research campaign (DLR, 2022). This was a research campaign that took place simultaneously with ISLAS 2022 in Kiruna, and was also targeting Arctic air mass transformation. Information on launch date and time for the radiosonde and dropsonde balloons is found in Appendix A, Table A.1.

3.6   Operational NWP model data

Results from the Norwegian operational numerical weather prediction (NWP) model AROME-Arctic have been utilized to supplement the CMET observations. Applications of Research to Operations at Mesoscale (AROME)-Arctic is a regional convection permitting NWP model for the European Arctic (Müller et al., 2017a). The model was adopted in 2015 by the Norwegian Meteorological Institute (MET-Norway), and currently serves as MET Norway's operational weather forecast system in the Arctic together with the Meteorological Cooperation on Operational Numerical Weather Prediction (MetCoOp) model for mainland Norway. AROME-Arctic is in close proximity to the MetCoOp model, and both are branches of the AROME based model configuration HARMONIE-AROME within the ALADIN-HIRLAM numerical weather prediction system (Müller et al., 2017b).

AROME-Arctic's model domain spans over a majority of the Nordic seas region. The model is non-hydrostatic and operates with a 2.5 km horizontal resolution, stacked on 65 vertical levels in a hybrid pressure format. The model generates hourly output and updates at a 3-hourly cycle, where 66- and 3 hourly deterministic forecasts are produced for every main cycle (00, 06, 12, 18 UTC), and intermediate cycle (03, 09, 15, 21 UTC)

respectively.

Forcing from lateral and upper boundaries are obtained from the European Centre for Medium Range Weather Forecast (ECMWF) high resolution global model. Initial conditions are achieved by the use of 3D-variational data assimilation for the upper atmosphere, while surface variables are assimilated through optimal interpolation. A more detailed description of the AROME-Arctic model and its characteristics can be found in (Müller et al., 2017a).

3.6.1   Model visualization

The AROME-Arctic model data was retrieved and visualized using the Weathervis visualization tool (Johannesen, 2021). This tool eases the retrieval of meteorological data from the THREDDS data server where MET Norway shares their data publicly. Weathervis provides plotting routines for the model data, and enables the user to adjust the plots by changing model run, domain, lead time, and adding additional information to the plots.

3.6.2   Model-CMET validation methods

Bias and accuracy are the two verification methods used here to validate AROME-Arctic and the measurements. Bias is described as the average correspondence between a forecast variable and the observations (Warner, 2010). This is equivalent to the mean error (ME) defined as,

$$ME = \frac{1}{n} \sum_{k=1}^{n} (x_k - o_k) = \overline{x} - \overline{o} \tag{3.11}$$

The accuracy is measured by the root mean square error (RMSE), Eq. 3.12, (Warner, 2010).

$$RMSE = \sqrt{\frac{1}{n} \sum_{k=1}^{n} (f_k - o_k)^2} \tag{3.12}$$

3.7   FLEXPART

The FLEXIble PARTicle (FLEXPART) Lagrangian particle dispersion model has been implemented to simulate one of the CMET-balloon flights. FLEXPART is an atmospheric Lagrangian particle dispersion model, written in FORTRAN code. It contains a great number of intended individual particles. The model was originally developed to calculate mesoscale and long range dispersion of hazardous substances, like for instance in association with a nuclear accident. However, FLEXPART has also been utilized in the modeling of a wide range of other atmospheric transport features, including the global water cycle (Stohl et al., 2005).

3.7.1 FLEXPART Simulation settings

Each particle represents a certain mass. FLEXPART can simulate the spread of passive tracers forward and backward in time. The latter enables users to identify air mass source regions, while the forward simulation provides the means for users to approximate future air mass pathways. Furthermore, unlike Eulerian models, Lagrangian models have no numerical diffusion related to computational grids. In Eulerian models, the numerical diffusion in the advection scheme is too high to properly project the shape of narrow plumes (Verreyken et al., 2019).

FLEXPART has a latitude-longitude-altitude grid. Nested horizontal grid is an option that can be chosen to excerpt higher resolution on specific parts of the domain. The tracers can be launched from a point, line, area or a volume. FLEXPART requires meteorological input data from numerical weather prediction models, through a three dimensional field of horizontal and vertical wind components, as well as temperature and specific humidity. With initial conditions from a weather model, it can run independently and operate with its own model settings. Here we use boundary data from AROME-Arctic.

3.7.2 FLEXPART-AROME

AROME is one of the regional models that supports FLEXPART. The FLEXPART-AROME configuration is based on FLEXPART-WRF. FLEXPART-AROME utilizes a Lambert-Conformal projection in the horizontal and has hybrid sigma levels projected on vertical levels that are Cartesian terrain following. The wind vector governing the transport of the particles is shown by Eq. 3.13 below,

$$v = \overline{v} + v_t + v_m \tag{3.13}$$

where $\overline{v}$ is the grid scale wind, and v_t and v_m are the turbulent and mesoscale wind fluctuations respectively. In the following are descriptions of some of the options that can be applied in FLEXPART.

3.7.3 Turbulence schemes

Turbulence is an important factor in determining particle transport on the sub grid scale. FLEXPART utilizes different physical parameterization schemes for turbulence in the atmospheric boundary layer, free atmosphere and mesoscale. First, for the atmospheric boundary layer (ABL) particles can be transported and mixed vertically. To model subgrid scale turbulence within ABL, a normal Gaussian approximated turbulence scheme is applied for stable and neutral conditions. As a result of downdraft areas having a greater horizontal extent than updraft areas, a skewed turbulence scheme was integrated for unstable convective boundary layers. Second, for the free atmosphere, FLEXPART represents turbulent fluctuations in terms of turbulent diffusivity. The mean displacement due to diffusivity is

$$\sigma_{xi} = \sqrt{2D_i dt} \tag{3.14}$$

where i represents the vertical and horizontal directions, and where D is the vertical and horizontal diffusivity.

3.7.4 Concentration calculation

For every time step the particle concentration inside the grid cells are computed by gathering the mass fraction of all the tracer particles and dividing them by the volume of the grid cell, as the following

$$C_{Ts} = \frac{1}{V} \sum_{i=1}^{N} (m_i f_i) \tag{3.15}$$

where V is the volume of the grid cell, N is the number of particles, m_i is mass, and f_i the fraction of the grid cell which the particles occupy. An illustration of how this fraction is assigned to the calculation is shown in Fig. 3.4. The concentration has then been used to find a weighted mean.
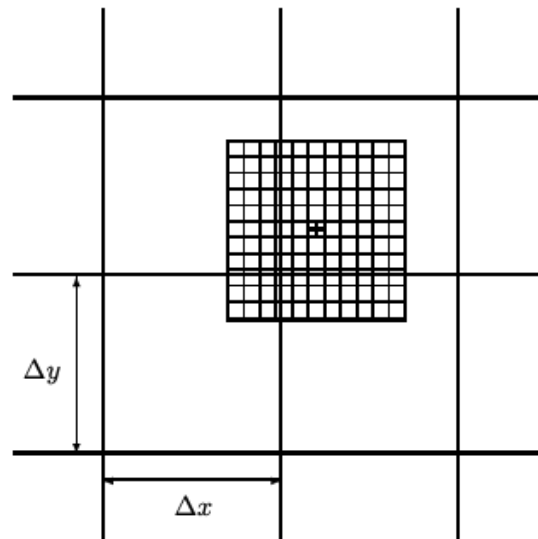

Figure 3.4: Schematic of a particle's mass distribution on the grid cells in FLEXPART. (Stohl et al., 2005, Fig. 1).

3.8 FLEXPART-CMET comparison

A statistical approach has been applied on the output results in order to find a representative particle trajectory for validation with the CMET. The weighted mean of the number of particles per grid cell has been calculated for every time step. The weighted mean is calculated as (Finch, 2009):

$$\mu = \frac{\sum_{i=1}^{n} w_i x_i}{\sum_{i=1}^{n} w_i} \tag{3.16}$$

Here μ is the weighted mean, and is calculated by adding all latitudes and longitudes x_i, multiplied with their specific weights w_i. The weights are taken from the concentration

field in the FLEXPART output. The advantage with this approach is that the densest grid cells are allowed to exhibit a greater impact on the latitude and longitude position of the particle trajectory.

AHTD calculation

The location of the values that correspond to the weighted mean are found and used to find a trajectory that represents air particle motion at an identical altitude as to the CMET balloon. Trajectory errors between the weighted mean based and the CMET trajectory can be given as the sum of all the incremental errors as (Riddle et al., 2006)

$$\vec{E}_i = \sum_{n=1}^{i} \Delta \vec{E}_n \tag{3.17}$$

where $\vec{E}_i$ is the total error of all $\Delta \vec{E}_n$ incremental trajectory errors. In order to find the distance between the modeled and observed trajectories, the Haversine formula was used (Veness, 2019):

$$a = sin^2 \left(\frac{\Delta \phi}{2} \right) + cos \phi_1 cos \phi_2 sin^2 \left(\frac{\Delta \lambda}{2} \right) \tag{3.18}$$

$$c = 2 \arctan 2(\sqrt{a}, \sqrt{1-a}) \tag{3.19}$$

$$d = Rc \tag{3.20}$$

Here latitude and difference in latitude between modeled and observed trajectories is given by ϕ_1, ϕ_2 and $\Delta \phi$ respectively. Longitude is given by λ, and Earth radius by the notation R, known to be 6371 km. The Haversine formula finds the shortest distance between two locations on the Earth surface. Here, this formula has been used to find the distance between the CMET and model trajectory. The distance is used in order to obtain an estimate on horizontal trajectory error, also referred as absolute horizontal transport deviation (AHTD) (Riddle et al., 2006).

3.9   Model set up

In total 3 forward simulations with the FLEXPART-AROME version 1.21 model were run (Table. 3.6). The simulations include the release of 250 000 air tracers, and were conducted with different forecast initializations and release points. The outputs were projected on a stereographic grid with 2.5 km horizontal resolution, and using vertical hybrid model levels retrieved from model level 10 to 64, which corresponds to 100-5000 m altitude. The sampling rate was set to 300 s where 30 min average concentration was written out. Input data was retrieved from AROME-Arctic with forecast base times in the period 25 Mar - 26 Mar 2022. Mean winds were used to force particle movement, and no schemes such as physical parameterizations, or deposition were activated. There was also no use of nested grids in the simulations.

Table 3.6: Overview of the conducted FLEXPART-AROME simulations.

Run	Forecast base time	Release time	Release point	Release height
1	25.03.22 18 UTC	20:01 UTC	77.53°N, 11.70°E	3000 m
2	26.03.22 00 UTC	03:00 UTC	74.83°N, 16.66°E	3000 m
3	26.03.22 00 UTC	03:00 UTC	74.54°N, 16.38°E	3000 m

The first simulation was run from 25.03.22 20:01 UTC to 26.03.22 11 UTC with 15 hourly time steps. Forecast initialization from 18 UTC the same day was used, corresponding to a two hour lead time during time of release. The particles were released from a point equal to the position of the CMET balloon at the maximum height during flight 2 at 3000 m, which was 77.53° N and 11.70° E. Simulation 2 and 3 were run from 26.03.22 03-17 UTC with forecast input from 03 UTC the same day, equal to a lead time of 3 hours at release. In simulation 2, the particles were released at 74.83° N and 16.66° E corresponding to the CMET flight track, while simulation 3 had particles released at 74.54°N and 16.38°E, corresponding to the track of the calculated 3000 m trajectory in simulation 1.

4. CMET-Fieldwork

4.1 CMET Launches

In the following chapter, a brief description of the launched CMET flights will be given. In total 6 CMET balloons were deployed during the ISLAS 2022 campaign. The CMET balloons were launched from the AWIPEV balloon hangar in Ny-Ålesund. All launches were carried out by Dr. Lars R. Hole and a field assistant between 24th of March and 4th of April 2022. The flights were constantly monitored by a crew in Kiruna, together with Paul B. Voss who issued the previously agreed commands. An overview of the flights can be found in Table 4.1, and a time line displaying the different balloon launches in Fig. 4.2.
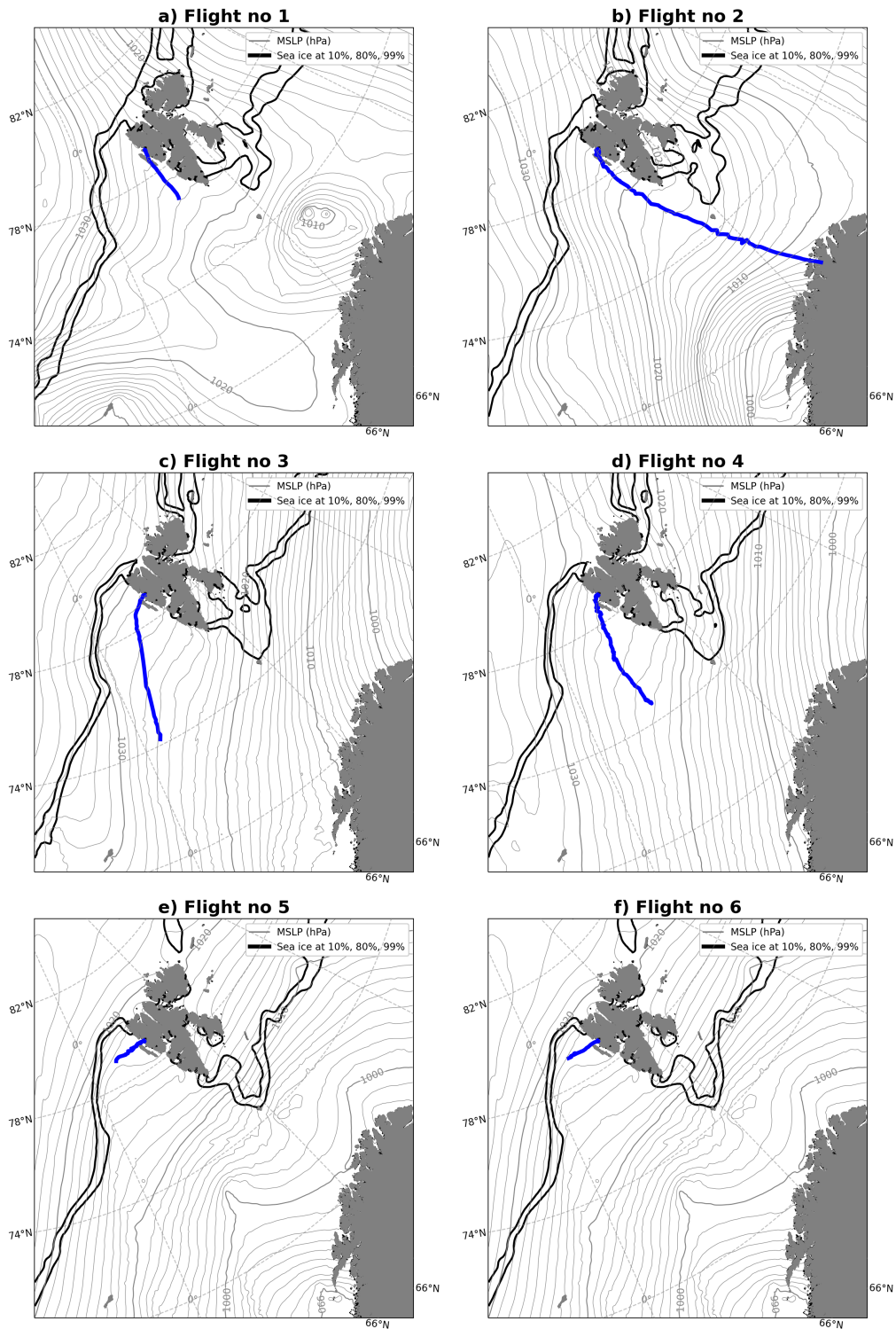
Figure 4.1: Flight paths for CMET flights a) 1. (24 Mar 2022), b) 2. (25 Mar 2022), c) 3. (28 Mar 2022), d) 4. (30 Mar 2022), e) 5. (4 Apr 2022), and f) 6. (4 Apr 2022) marked by the blue lines. Sea ice (%) and MSLP (hPa) during time of launch are indicated by thick black and grey lines respectively.

4.1.1 Flight 1. (24 Mar 2022)

The first CMET balloon was launched 24 March 14:54 UTC. Since this was the first launch of the campaign it was a test flight. In total 7 commands were transmitted. First an ascend command to 1400 m, with a maximum ascent rate of 0.8 m/s to prevent the pump going too quickly. The balloon was set into profiling mode between 1300 and 1500 m, later between 2000 and 2400 m. The balloon however, only descended to 2200 m, before it was set to profiling mode between 1900 and 2300 m. The balloon was terminated 25 Mar 00:30 UTC after a flight time of 9,5 h, as a result of loss of height, probably due to icing from mixed phase clouds (Fig. 4.1a).

4.1.2 Flight 2. (25 Mar 2022)

CMET balloon no 2 took off 25 March 14:58 UTC. The objective of the flight was to keep the balloon floating at a safe altitude for as long as possible in order to provide data for later comparison with FLEXPART. 17 commands were issued during the course of the flight. First, an ascend command to 2300-2700 m was accomplished, followed by a transmission command to change data transmission to every 15 minutes with an acquisition rate every 3 minutes. Later, different ascend commands within the range of 2500 and 3500 m were completed in order to keep the balloon at a floating altitude above the boundary layer. A profile command between 400 and 2500 m was activated before a last ascend command was done. Subsequently, we emptied the helium tank, in preparation for a controlled landing on Kvaløya, due to restrictions with an ongoing military campaign on the Norwegian mainland. The balloon was terminated at 26 Mar 11:34 UTC after flying for 20 h (Fig. 4.1b). Fortunately, the CMET balloon was found and returned to UiB 5 months after.

4.1.3 Flight 3. (28 Mar 2022)

The third CMET balloon was launched 28 March 22:50 UTC, in order to carry out vertical profiling of the boundary layer. 17 commands were completed. First, an ascend command was given to take the balloon to 1400-1600 m altitude range. This was followed by a GPS hotfix command before two new ascend commands were issued in order to lift the balloon up to 2400-2600 m. Later, we issued deep profiling commands between 400 and 2800 m because the balloon was operating in a cloud free area and the risk of encountering clouds was low. This was followed by a set of descend and ascend commands with different transmission rates. Then, after a flight time of 19.5 h (Fig. 4.1c), the balloon had to be terminated due to battery outage, which occurred 29 Mar 18:24 UTC (Table 4.1).

4.1.4 Flight 4. (30 Mar 2022)

CMET balloon no 4 was deployed 30 March 02:14 UTC. Like balloon no 3, it was going to target the boundary layer development through deep profiling. 18 commands were undertaken. First, an ascent command to 1400-1600 m was sent, where the higher limit was later adjusted to 2200 m. A deep sounding was made when we sent the balloon down to 400-600 m. We thereafter, positioned the balloon for simultaneous profile comparison with a HALO dropsonde (Fig. 4.2) launch nearby. A joint consequence of icing and battery outage forced us to terminate the balloon on 31 March, at 01:12 UTC after a flight time of approximately 23 h.

Table 4.1: Summary on key information of the CMET flights on date, time, flight number, flight objective and termination cause.

Date	Time (UTC)	Flight no.	Flight objective	Termination Cause/Remarks
24 Mar	14:54-00:30	1	Test flight	Icing
25 Mar	14:58-11:12	2	FLEXPART validation	Forced descent
28 Mar	22:50-18:24	3	Profiling	Battery outage
30 Mar	02:14-01:12	4	Profiling	Icing/battery outage
04 Apr	02:06-09:06	5	Dual launch	Leakage/bursting (no solar panel)
04 Apr	02:06-11:34	6	Dual launch	Battery outage (no solar panel)

4.1.5   Flight 5. and 6. (4 Apr 2022)

CMET flights no 5 and no 6 started on 4 April 02:06 UTC. The two final balloons were launched simultaneously in order to perform a dual launch experiment to study atmospheric dispersion. In contrast to the other balloons, these two balloons were not equipped with solar panels (Table 4.1). Four commands were issued to flight no 5, while 9 were sent to flight no 6. Ascend commands to 1800-2200 m were sent to both balloons. However, flight no 5 experienced leakage and continued to 4000 m. As a result, CMET 5 was terminated the same day at 09:06 UTC after a flight time of 7 h in order to avoid bursting and ensure a data friendly descent. CMET balloon no 6, however, continued at 1800-2200 m altitude. After a flight time of 9.5 h, flight 6 was terminated 11:34 UTC when battery power ran out (Fig. 4.1f).
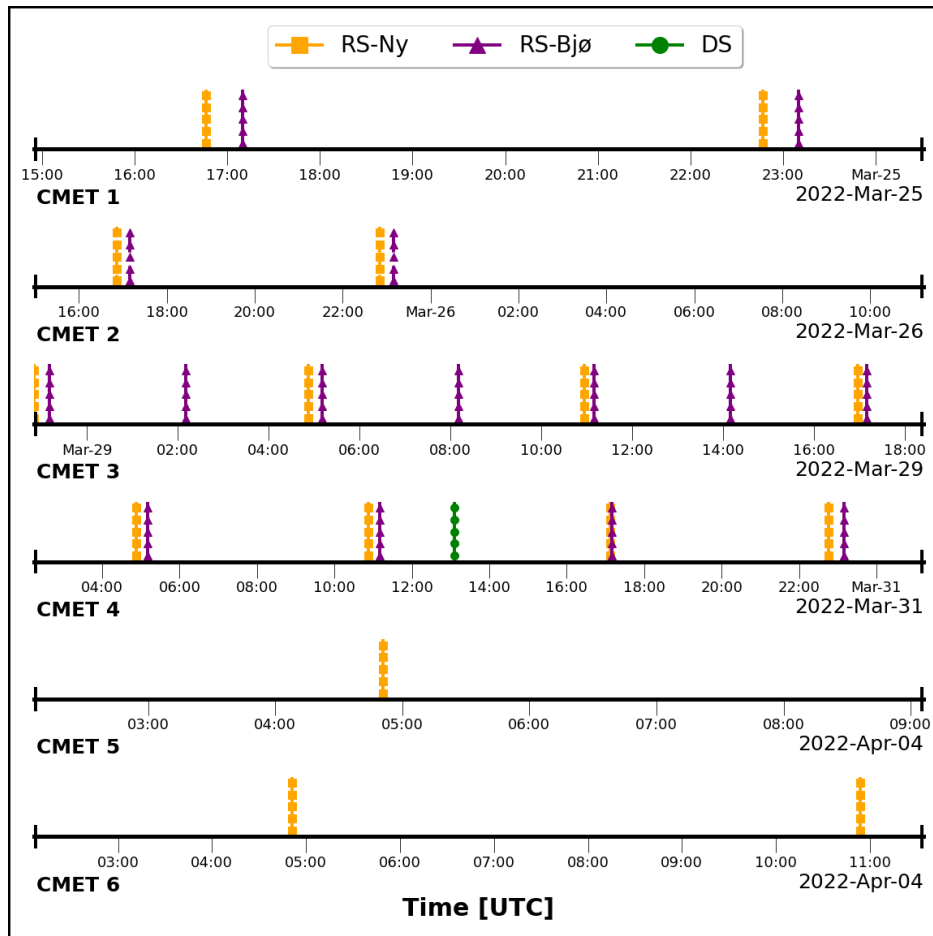
Figure 4.2: Time lines of CMET flight 1, 2, 3, 4, 5 and 6 together radiosonde launches from Ny-Ålesund (yellow), radisonde launches from Bjørnøya (purple) and dropsonde launch (green).

5. Results

The analysis consists of two parts. First, measurements from CMET balloon no. 2 and 4 are analyzed together with AROME-Arctic, radiosonde and dropsonde balloon data to identify the change in atmospheric bulk properties. Second, results from simulations of air mass transport by FLEXPART-AROME are presented together with data from CMET balloon 2.

5.1 CMET and radiosonde launches

Below follows a presentation of the mean difference between modeled and observed launch profiles in Ny-Ålesund. The differences between CMET launch and model, and between the nearest radiosonde launch and model below 2000 m height after launch in Ny-Ålesund for all the 6 CMET launch days (Fig. 5.1). The investigated variables include potential temperature, (Fig. 5.1 a), specific humidity (Fig. 5.1 b), wind speed (Fig. 5.1 c), and wind direction (Fig. 5.1 d) and are mean values for every 100 m height interval.
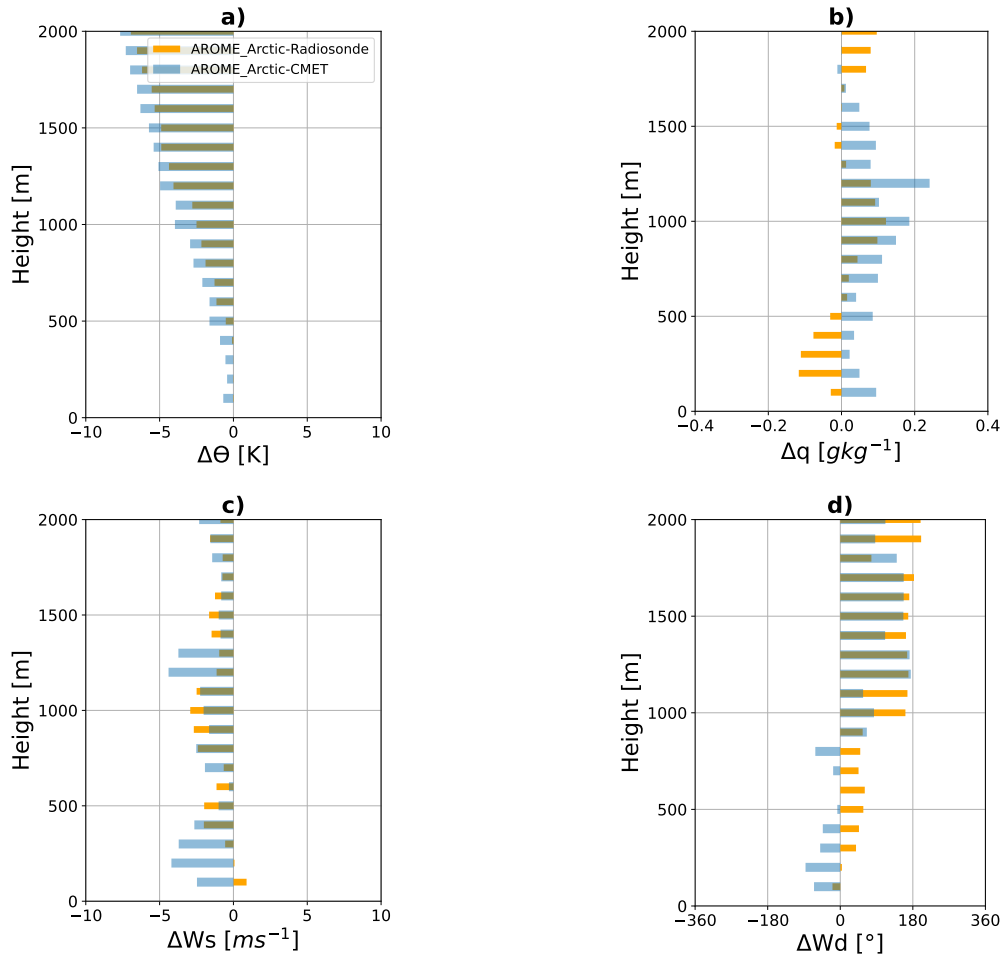

Figure 5.1: The average difference between CMET and Arome-Arctic (orange), and CMET and radiosonde (blue) in terms of potential temperature (a), specific humidity (b), wind speed (c) and wind direction (d) for every 100 meter in Fig. 5.9.

The offset between radiosonde and CMET measurements are relatively intact. Negative

difference is evident for potential temperature and wind speed (Fig. (5.1 a, c), leading to a mean difference of -5.50 K and -4.77 K for the CMET and radiosondes respectively (Table 5.1). For specific humidity, there is a positive difference of 0.10 gkg^{-1} for the radiosonde and 0.05 gkg^{-1} for the CMET profiles, while for wind speed both CMET and radiosonde display negative differences of -2.88 and -1.60 ms^{-1}. The CMET and radiosonde show greater variations in terms of wind direction, however (Fig. 5.1 d).

Table 5.1: Mean differences between AROME-Arctic and all CMET launch profiles and nearest radiosonde launch profiles.

	Potential temperature (°C)		Specific humidity (gkg^{-1})		Wind speed (ms^{-1})	
	CMET	RS	CMET	RS	CMET	RS
Mean	-5.50	-4.77	0.10	0.05	-2.88	-1.60

5.2 Flight 4 (30-31 March 2022)

In the following section, a case study of CMET flight 4 will be given. This includes an overview of the synoptic scale situation, time integrated vertical cross sections of observations and forecast, as well as vertical profiles.

5.2.1 Synoptic situation

A brief overview of the atmospheric situation from 30 Mar 2022 is shown in Fig. 5.2. The figure is valid for 12 UTC (mid flight) and the illustrated parameters are boundary layer height (Fig. 5.2a), top of atmosphere outgoing long wave radiation (Fig. 5.2b), integrated liquid water and ice concentration (Fig. 5.2c) as well as cold air outbreak index (Fig. 5.2d). In addition, Fig. 5.2a, Fig. 5.2c and Fig. 5.2d showcase the isobars for mean sea level pressure that are elongated along every 1 hPa interval. Added information such as vertical velocity and position of the marginal ice zone (MIZ) are included in Fig. 5.2a and 5.2d respectively. All plots contain the flight track of the CMET balloon that is highlighted with overlying crosses appearing at an hourly frequency.
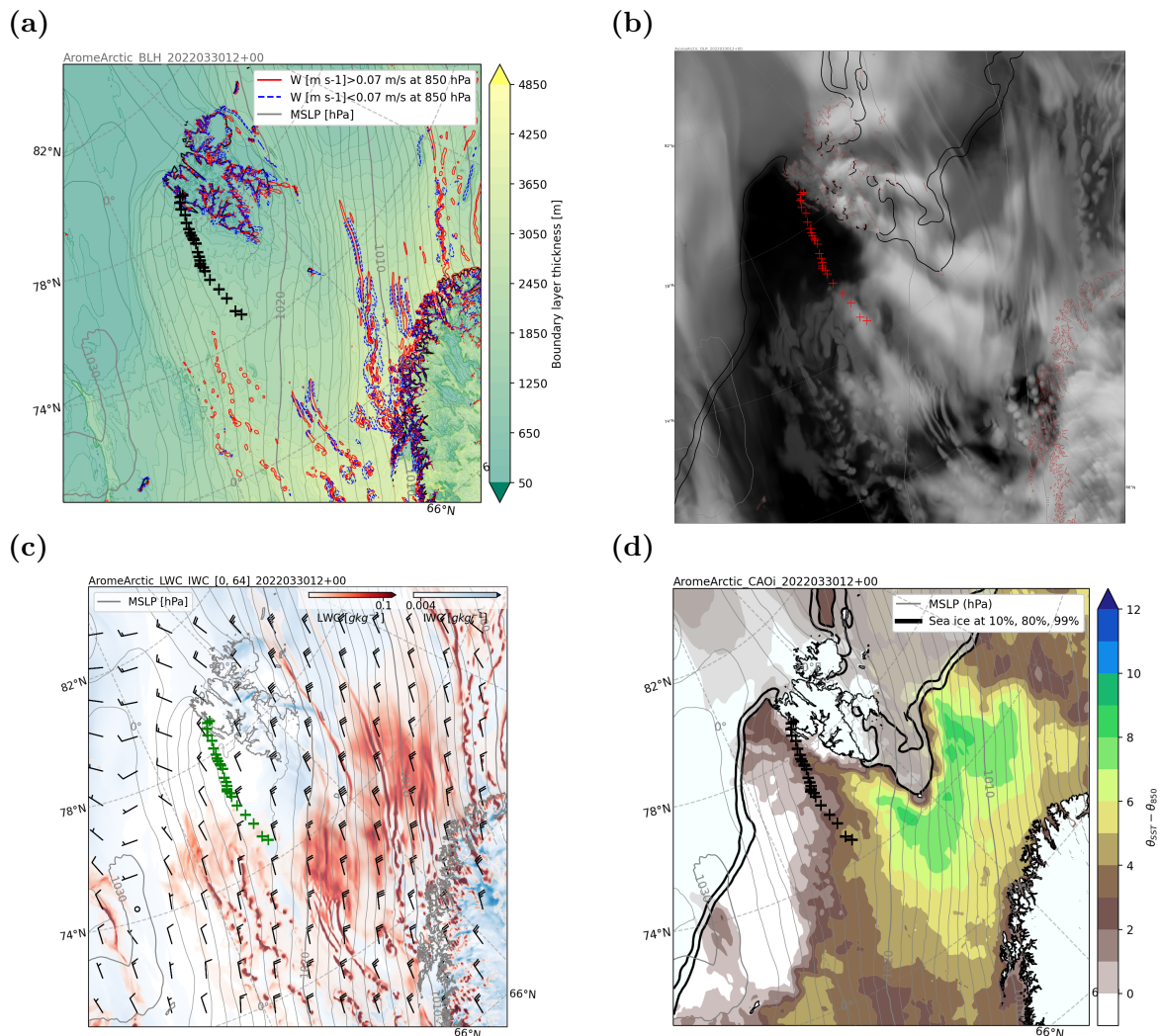
(a)

(b)

(c)

(d)

Figure 5.2: Synoptic weather situation from AROME-Arctic valid on 30 March 2022 12 UTC at +00 h lead time. Shown parameters are: Boundary layer height and vertical velocity (a), simulated top of atmosphere outgoing long wave radiation (b), integrated liquid water- and ice concentration and 3000 m wind (c) and cold air outbreak index (d). Mean sea level pressure and sea ice extent are denoted by thin grey contours and thick black lines respectively. The crosses show the CMET-balloon's position at an hourly rate.

An area of relatively high pressure can be seen to the north west of Jan Mayen (Fig 5.2a). As a result, there is a decreasing pressure gradient in the zonal direction, establishing a north easterly geostrophic flow field. Regions of enhanced vertical velocities appear to coincide roughly with dots and lines of distinguished liquid water concentration, hinting of deep convective activity and precipitation (Fig. 5.2a-c). The noteworthy convective rolls can also be seen by the red lines that gradually get disassembled into broken up cells (Fig. 5.2c).

As seen in Fig. 5.2b, the CMET balloon advanced into a cloud free area in the lee of Svalbard, most likely entering through an area of generally low wind speeds because of the greater gap in isobars to the south west of Svalbard. One can also see the archipelago is trapped in the sea ice (Fig. 5.2d), with only open sea access from the west coast. In addition, the sea ice cover is prolonged to the south of Svalbard down towards Bjørnøya.

29

The balloon trajectory slightly started to encounter a cyclonic curvature at the end of the flight, which perhaps can indicate the spin up of a mesocyclone.

5.2.2 Vertical cross sections

Time interpolated vertical cross sections are used to show the modeled evolution of the moving air mass along the CMET flight trajectory. The vertical cross sections show a comparison of the CMET balloon and the AROME-Arctic model. In Fig. 5.3 vertical cross sections depicting the CMET observations on AROME-Arctic background for potential temperature, specific humidity, wind speed and wind direction are shown. The height corresponds to vertical model levels between 28 and 65 in AROME-Arctic, and are retrieved at an hourly frequency for the nearest model grid point to the CMET's position. The output has then been converted to a time-altitude plane which follows the CMET balloon flight path, with regular updates every time there is a new forecast issued from AROME-Arctic. The same color scale is utilized for both CMET and AROME-Arctic forecasts for easier comparison.
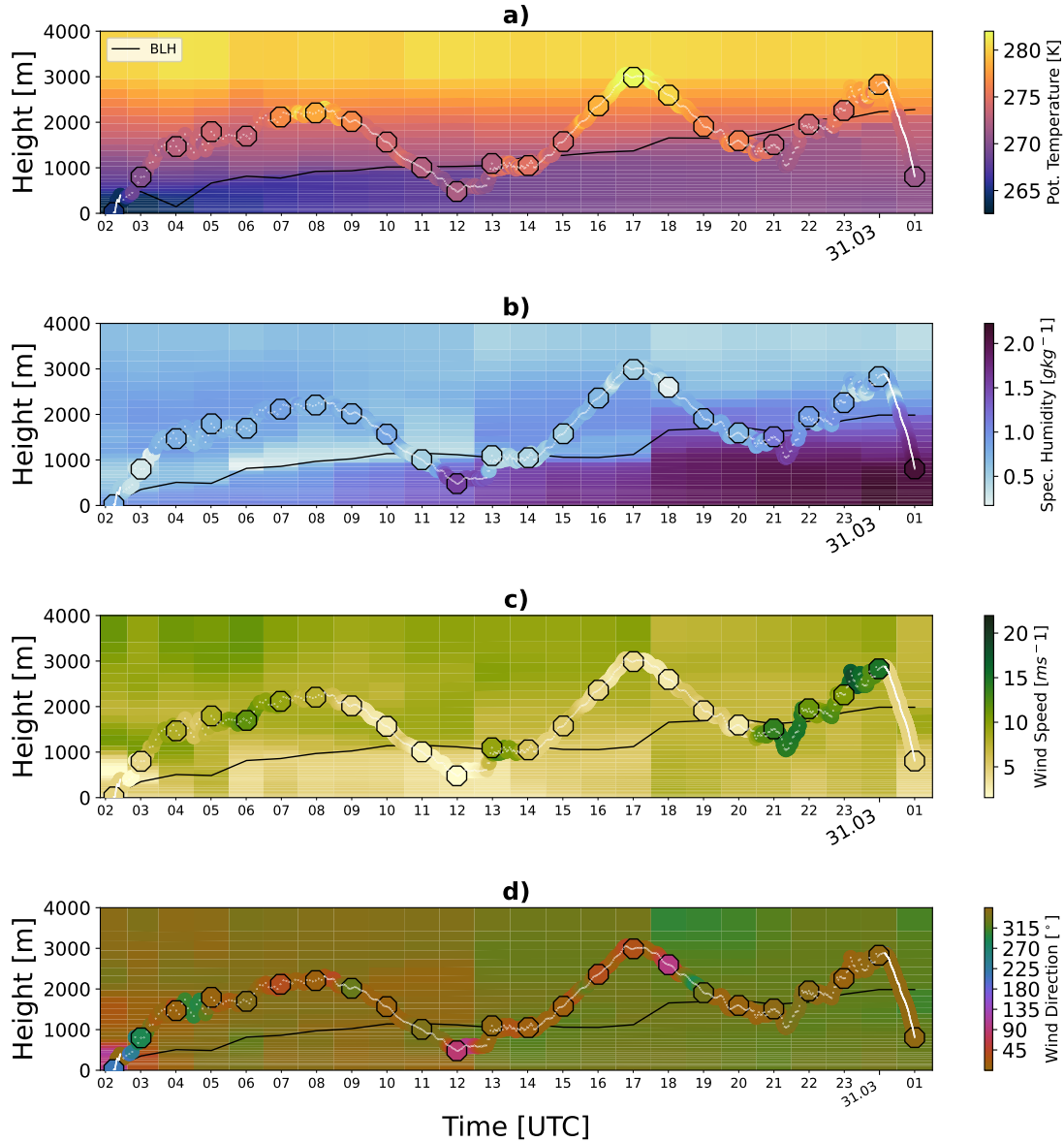
Figure 5.3: Time integrated vertical cross sections of different variables: a) potential temperature (K), b) specific humidity (gkg^{-1}), c) wind speed (ms^{-1}), and d) wind direction (°) from flight 4, with continuously updated AROME-Arctic forecast background. The flight path (white line) and the model evaluated positions (black circles) are highlighted. The black circles are also indicated every hour to keep track of the balloon's altitude. Simulated boundary layer height (BLH) is shown by the black line.

Generally, the CMET shows good agreement with AROME-Arctic. The CMET is seen undergoing three cycles of soundings, where increasing lower atmospheric potential temperature and specific humidity is encountered by both AROME-Arctic and CMET (Fig. 5.3a-b), which is as expected during mCAOs. However, even though a lower level inversion near 1000 m is represented by both, the CMET also detects a secondary inversion near to 2000 m during the first ascent (Fig. 5.3a). The CMET also captures this inversion close to 3000 m at a later stage of the flight (Fig. 5.3a). AROME-Arctic also finds a narrow dry layer at approximately 1000 m (06 UTC) that is related to the previously mentioned lower inversion (Fig. 5.3 b). This feature is also represented by the

CMET, but the vertical extent of the layer appears to be larger in reality than what was predicted by the model (Appendix C, Fig. C.1)

For a more quantitative comparison, time series of potential temperature, specific humidity and wind speed are shown (Fig. 5.4). Analogous to Fig. 5.3, the depicted parameters are collocated in space and time, representing the black circles from the vertical cross sections. This gives a more quantitative picture of the differences between CMET and AROME-Arctic surrounding the CMET balloon. Furthermore, to obtain an overview of the magnitude of any potential uncertainty with respect to initial conditions, the non updated forecast issued right before launch has been included in Fig. 5.4. The updated and non updated forecasts are here referred to as "Latest time" and "Initial time".
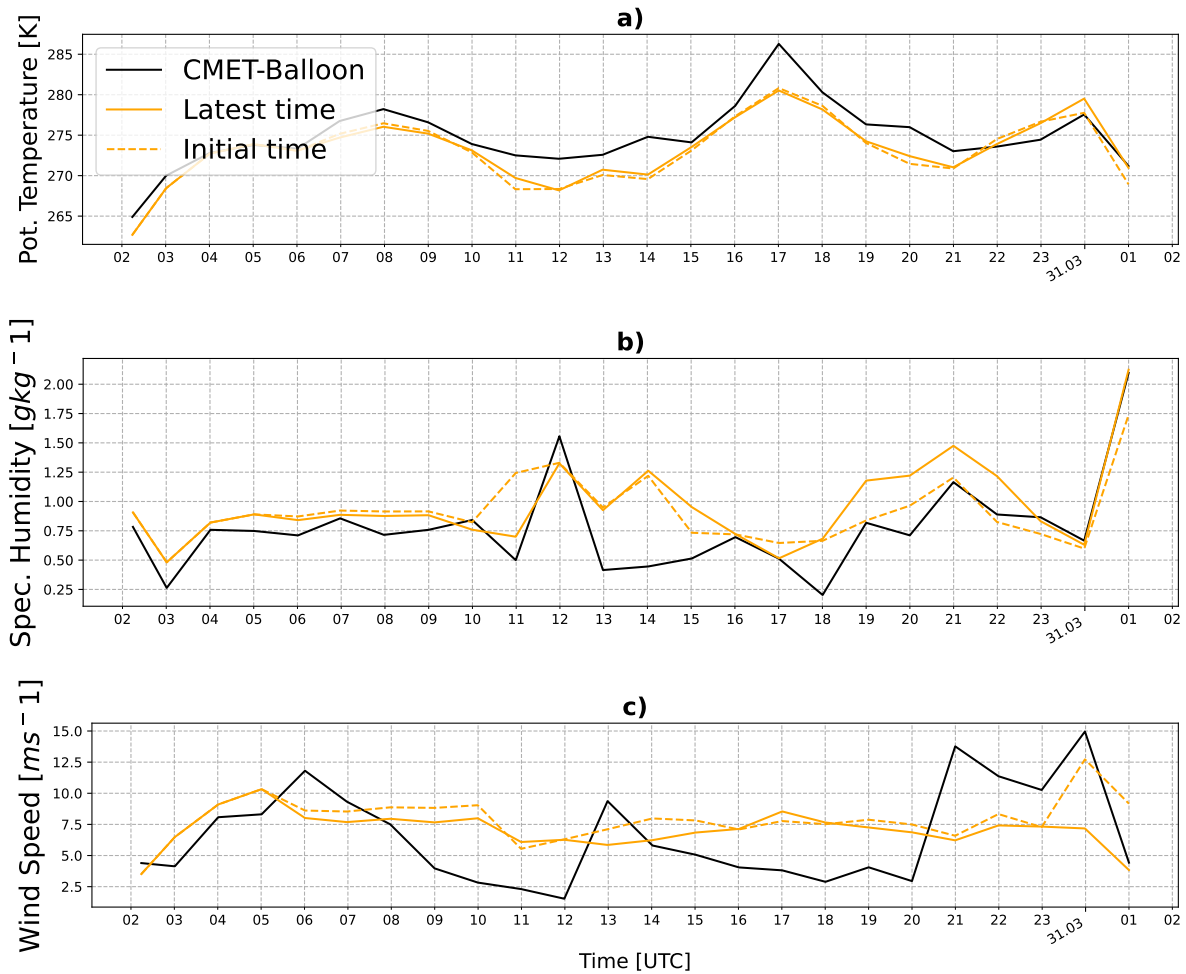

Figure 5.4: Time series of: a) potential temperature (K), b) specific humidity (gkg^{-1}), and c) wind speed (ms^{-1}) for the CMET 4 flight and AROME-Arctic forecasts issued at Initial time: 30.03.2022: 00 UTC (dashed orange line), and at Latest time: 30.03.2022: 00, 06, 12, 18, as well as 31.03.2022: 00 UTC (solid orange line) for the nearest model grid cell. CMET observations are indicated by the black line.

Overall, the CMET observations are in accordance with the issued forecasts, but discrepancies remain visible (Fig. 5.4). Both forecast times underestimate potential temperature until the evening (22 UTC) where a better agreement is achieved (Fig. 5.4a). Secondly, both forecasts appear nearly similar, arguing for good confidence in the prediction of temperature and stability by AROME-Arctic. Similar can be said about wind

speed, where there are relatively small variations between the model runs, exhibiting limited in-flight vertical wind shear. On the contrary, CMET shows a greater altitude dependent wind speed variability. The most pronounced differences however, are seen in humidity. Specific humidity is mostly overestimated by the model, with the largest gradients showing up at midday (13-19 UTC). Interestingly, the latest forecast substantially exaggerates the moisture content after 18 UTC. For a qualitative description of the differences, bias and accuracy were calculated. A summary of mean, bias, and root mean square errors of the parameters in Fig. 5.4 is provided in Table 5.2.

Table 5.2: Mean, bias and root mean square error (RMSE) for potential temperature (K), specific humidity (gkg^{-1}) and wind speed (ms^{-1}) from CMET and AROME-Arctic Initial and Latest time forecasts along CMET4-flight track.

	Potential temperature (K)		Specific humidity (gkg^{-1})		Wind speed (ms^{-1})	
	Initial	Latest	Initial	Latest	Initial	Latest
Mean	272.97	273.19	0.91	0.96	7.91	7.06
Bias	-1.76	-1.54	0.14	0.19	1.37	0.52
RMSE	2.55	2.38	0.30	0.30	3.63	3.78

Examination of Table 5.2 affirms what was observed in Fig. 5.4. AROME-Arctic experiences a negative bias for potential temperature in both runs of -1.76 and -1.54 K, whereas a positive bias emerges for humidity and wind speed. A tendency of decreasing bias amid the forecasts appears true for all parameters except humidity, which increased slightly from 0.14 to 0.19 gkg^{-1}. This can essentially be viewed as result of the sharp contrast in the predicted humidity field between the different forecast initializations on the latest time (Fig. 5.4). In relation to RMSE, there is a minor decrease for potential temperature, no changes for humidity, while for wind speed there is a slight increase from 3.63 to 3.78 ms^{-1}. Principally, this can be explained by the high variance in the wind speed data from the CMET (Fig. 5.3).

5.2.3 Multiple vertical profiles

The humidity gradient obtained by the forecast could have originated from low predictability. On the other hand, misrepresentation of the model might also be a factor, as one would think that two air masses with different properties are mixed. To investigate this, observations from a dropsonde profile in close proximity to the CMET balloon are considered. In Fig. 5.5 the location of several soundings undertaken during the course of flight 4, including profiles from the CMET, radiosondes in Ny-Ålesund and Bjørnøya, and the HALO dropsonde is shown.
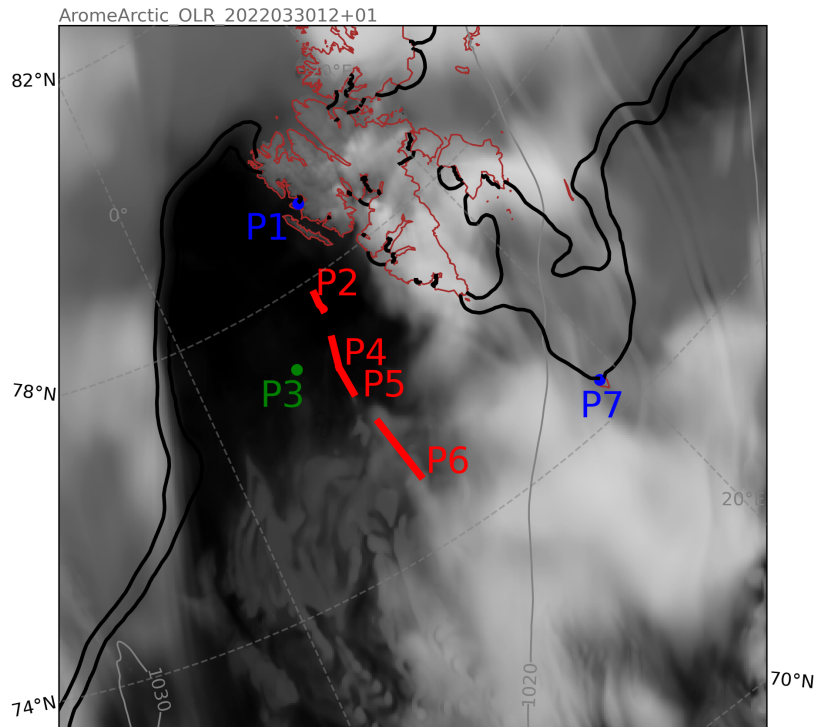
Figure 5.5: Location of the considered vertical profiles from CMET (red), radiosonde (blue) and dropsonde (green) launched at different time slots. The background shows model simulated cloud content initialized at 30.03.2022 12 UTC with 1 h lead time.

Since the CMET balloon used a longer time to undergo a vertical sounding, the horizontal range is longer, which explains why the CMET profiles are marked by lines and not dots (Fig. 5.5). Simulated cloud layer, mean sea level pressure and sea ice extent is valid for the time of the dropsonde launch (P3) at 13 UTC. Profiles of specific humidity are shown below (Fig. 5.6). The colors correspond to the type of balloon, similar to Fig. 5.5. Time of profiles is displayed starting from 05 UTC and ending at 23 UTC on 30 March 2022.
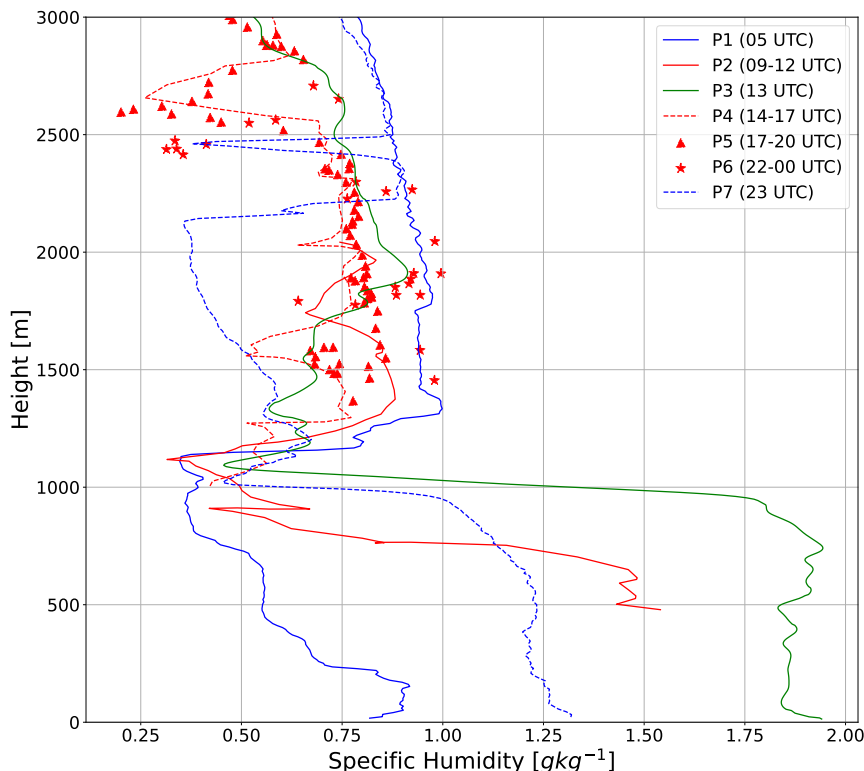
Figure 5.6: Vertical profiles from 30 Mar 2022 of specific humidity from CMET balloon (red), radiosondes (blue) and dropsonde (green).

Variations are noticeable between the profiles in Fig. 5.6. A low level humidity inversion is seen for P1, followed by a stronger humidity inversion above at approximately 1400 m. From P1 to P2, there is an increase in lower level specific humidity. From 1000-1200 m, however, the variations are negligible. The highest observed specific humidity is seen in P3 (dropsonde profile) with humidity values approaching 2 gkg^{-1} below 1000 m. The following CMET profiles (P4, P5, P6) did not extend below the 1000 m altitude, and consequently did not reproduce the same humidity values found in P3 and P4. However, recalling back from Fig. 5.3, there appeared to be higher humidity observed by the CMET balloon at 21 UTC, suggesting that higher humidity was present in the period between P5 and P6 which is not shown here. Fig. 5.6 also unveils a mixed layer along the CMET balloon track. The last profile (P7) from 23 UTC however, shows decreased lower layer humidity compared to P2 and P3.

5.3   Flight 2 (25-26 March 2022)

In this section, an emphasis will be put on CMET flight no 2. This particular CMET balloon sustained the longest flight during the campaign and was the only balloon that managed to reach mainland Norway. Equivalent to Flight 4, a comprehensive analysis of the synoptics, vertical profiles and model verification is performed.

5.3.1 Synoptic situation

Fig. 5.2 prescribes the atmospheric conditions from AROME-Arctic at midnight on 26 March, with the same parameters as in Fig. 5.2 shown.
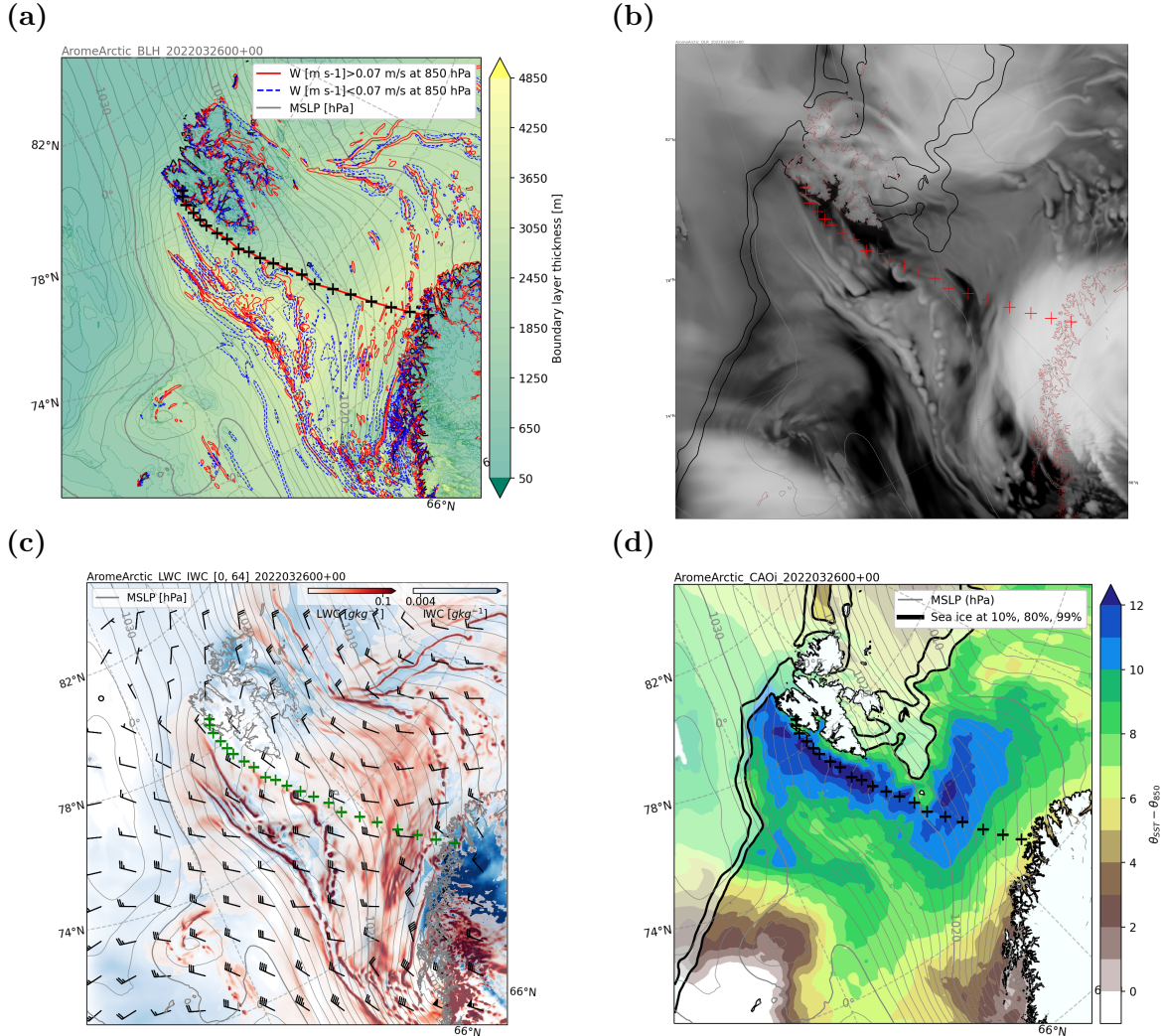
(a)

(b)

(c)

(d)

Figure 5.7: Synoptic weather situation from AROME-Arctic valid on 26 March 2022 00 UTC at +00 hour lead time. Shown parameters are: Boundary layer height and vertical velocity (a), simulated top of atmosphere outgoing long wave radiation (b), integrated liquid water- and ice concentration (c) and cold air outbreak index (d). Mean sea level pressure and sea ice extent are denoted by thin grey contours and thick black lines respectively. The crosses show the CMET-balloon's position at an hourly rate.

The synoptic setup on this day is roughly comparable to what was seen during CMET flight 4, where a high pressure system developed to the north east of Jan Mayen (Fig. 5.7). In company with a sharp zonal pressure gradient, strong outflows of Arctic air are induced, advecting the CMET in a southerly direction. Gradually, the center of the high pressure gets displaced towards Scandinavia (not shown here), which enforced a strengthened easterly drift on the CMET. Noteworthy is also the increasing wind speed acting on the CMET as it bypasses the lee of Svalbard, visible from the increased gaps on the trajectory and the wind barbs (Fig. 5.7c).

From Fig. 5.7b, three main areas with large horizontal extent of cloud cover can be seen.

The most prominent is situated above northern Scandinavia, which from Fig. 5.7c can be seen in association with a precipitating front due to the high concentration of ice. The second is located to the west of the high pressure center near Jan Mayen, and the last sits over the sea ice north of Svalbard. To the south of Svalbard, multiple bands of mixed phase stratocumulus and open convective cells develop along the geostrophic flow field as the offshore winds intensify downstream (Fig. 5.7c). Additionally, possible remnants of a polar mesocyclone that developed on one of the previous days can be spotted outside the Norwegian coast in the southernmost part of the domain (Fig. 5.7c-d).

Areas with enhanced boundary layer height in AROME-Arctic appear to possess good correlation with the areas containing convective cells and significant vertical velocities. Moreover, the model anticipates close resemblance between positive and negative vertical velocities (Fig. 5.7a). This is completely expected as the convective cells often produce narrow strong updrafts that are surrounded by larger downdraft regions. The CAO index is positive over almost the entire domain, with a pronounced maximum reaching 12 degrees in $\theta_{SST} - \theta_{850}$ outside the west coast of Svalbard, seen from Fig. 5.7d. Albeit the enhanced lower level static instability that one would assume here, clear sky and calm conditions were predicted for the same area. Also worth mentioning is the shift in sea ice that seems to be partially displaced between 26 Mar (Fig. 5.7) and 30 Mar (Fig. 5.2).

5.3.2 Radiosonde observations

For additional information on the atmospheric situation, thermodynamic profiles from Ny-Ålesund and Bjørnøya have been looked into. In Fig. 5.8, temperature, dew point temperature and wind data are retrieved from two Ny-Ålesund and two Bjørnøya soundings and plotted on Skew-T log-P diagrams. Wind barbs illustrating speed and direction are included in Fig. 5.8 and show average values over every 100 consecutive measurements.
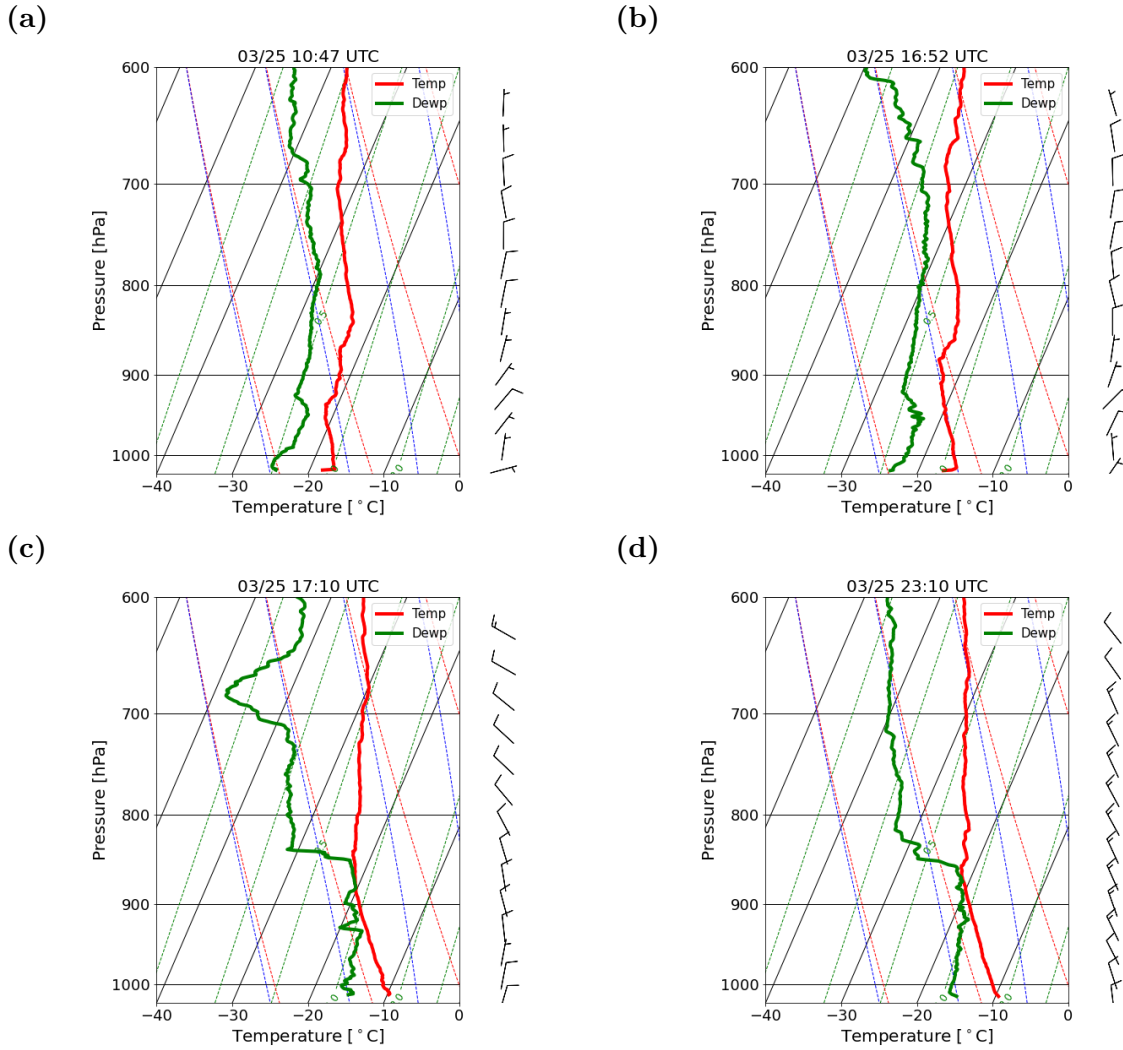
(a)

(b)

(c)

(d)

Figure 5.8: Skew-T log-P-diagram of radiosonde observations in Ny-Ålesund and Bjørnøya taken from 25.03.2022. Dry adiabatic lapse rate, moist adiabatic lapse rate and constant saturation mixing ratio are indicated by thin red, blue and green lines respectively. Temperature and dew point temperature is shown by the thick red and green lines, with wind barbs to the right. The displayed profiles show measurements from Ny-Ålesund at 10:47 UTC (a), and at 16.52 UTC (b), and from Bjørnøya at 17:10 UTC (c), and at 23:10 UTC (d).

The two locations show two different atmospheric situations with small internal variations. After inspecting the Ny-Ålesund soundings in Fig. 5.8a and Fig. 5.8b, one initially see that the both soundings facilitate a constant gap between temperature and dew point temperature, strongly suggesting the presence of dry air masses. A low level inversion hints of a near surface stable boundary layer. Winds from different directions can be seen as expected due to the complex topography around Ny-Ålesund. Common to both soundings is that no remarkable change in atmospheric conditions were observed.

Turning the attention over to Bjørnøya (Fig. 5.8c-d), higher surface temperature and humidity is seen. The intersection between the temperature and dew point temperature curve lies close to 900 hPa, which favors a relatively low cloud base. This is consistent with what the model predicted in Fig. 5.7. With regard to wind, the wind speeds are higher and have a northwesterly direction. A directional wind shear from north to north-

west was captured in the afternoon (Fig. 5.8c), but turned to a constant northwesterly direction in the evening, although accompanied by higher wind speeds (Fig. 5.8d).

Evaluating the difference between the two locations (Fig. 5.8a-d), however, we notice that from top to bottom there is a notable increase in temperature and dew point temperature at 850 hPa. Whilst from 850 hPa and beyond, there appears to be a slight increase in temperature and a considerable decrease in humidity, where the latter one could be related to the dry out of the low level humidity inversion advecting into Ny-Ålesund.

5.3.3   CMET launch profile compared to radiosonde and model

Since the profiles from Ny-Ålesund show little temporal variation on 25 Mar, it was decided to use one of the profiles in direct comparison with the deployed CMET during ascent. The chosen sounding corresponds to Fig. 5.8b. In addition, vertical profiles extracted from AROME-Arctic have been applied. Hence, Fig. 5.9 show vertical profiles of CMET and radiosonde observed as well as modeled potential temperature, specific humidity, wind speed and wind direction from Ny-Ålesund. As a result of minor inconsistencies in the CMET's ascent rate due to its lessened ability to penetrate through stronger stratified layers, the displayed CMET profiles only show the averaged quantity of every 100 meters between the surface and 3000 meters. Consequently, this would spark deviations in the balloons' horizontal flight paths.
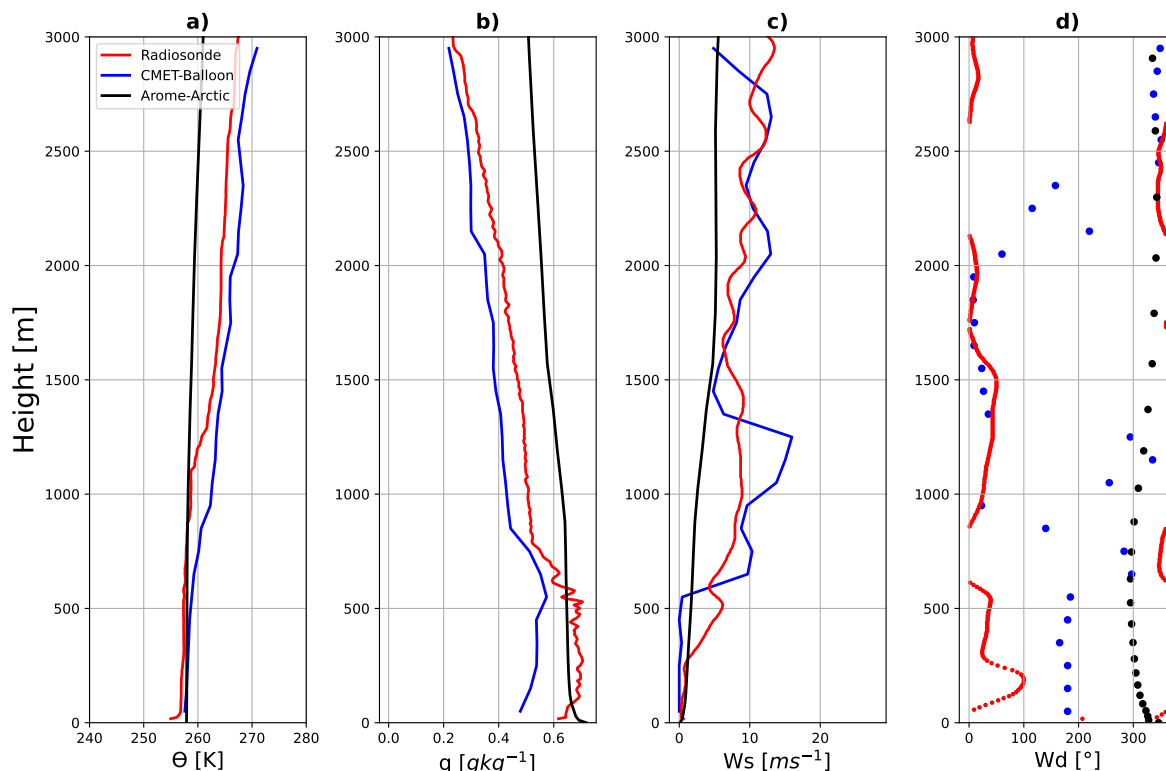

Figure 5.9: Vertical profiles from Ny-Ålesund on 25 Mar 2022 of potential temperature (a) in K, specific humidity (b) in gkg^{-1}, wind speed in ms^{-1} (c) and wind direction in °(d). CMET-balloon (blue) and radiosonde (red) were launched at 14:54 UTC and 16:46 UTC respectively. The forecast from AROME-Arctic (black) was initiated at 25 Mar 2022 12 UTC with a lead time of +03 hours (15 UTC).

The balloons and model profiles show different degrees of variations (Fig. 5.9). At first sight the profiles show good agreement, but closer inspection brings to light differences, not only between CMET and radiosonde, but also between the model and the radiosonde. Potential temperature seems partially underestimated by the model, whereas the balloons capture an increase in potential temperature with the highest increase from the CMET balloon (Fig. 5.9a). Apparently the model doesn't recreate this stability increase, but rather accommodates a more neutral vertical profile.

With relation to specific humidity, the modeled profile appears overestimated (Fig. 5.9b). Below 500 meters, a sufficient correspondence is achieved. Nevertheless, from there on, humidity declines more rapidly with height for the two balloons than what is anticipated by the model. Near the surface the model sees an increase in specific humidity that the CMET doesn't detect, nor does the radiosonde. This discrepancy could indicate how sensitive the launch site is to influence from the nearby Kongsfjord.

Although AROME-Arctic reproduces strengthening wind speed with height, similar to the observations, the wind speed, however, is severely under predicted (Fig. 5.9c). Based on the CMET, and especially the radiosonde, there is a vertically alternating wind speed that is not foreseen by model, which possibly could originate from gravity waves. Lastly, there is a substantial mismatch found in wind direction on the CMET (Fig. 5.9d). This is as a result of the constant variations between 0 and 360°.

5.3.4 CMET and AROME-Arctic cross sections

The results from the ascent profiles do not necessarily represent the whole CMET-flight. To investigate the observations of the much more remote seas to the south of the Svalbard archipelago, vertical cross sections with the balloon on model background were made. Similar approach as for flight 2 has been applied here. Fig. 5.10 shows a comparison of the CMET balloon flight path with AROME-Arctic background for potential temperature, specific humidity, wind speed and wind direction.
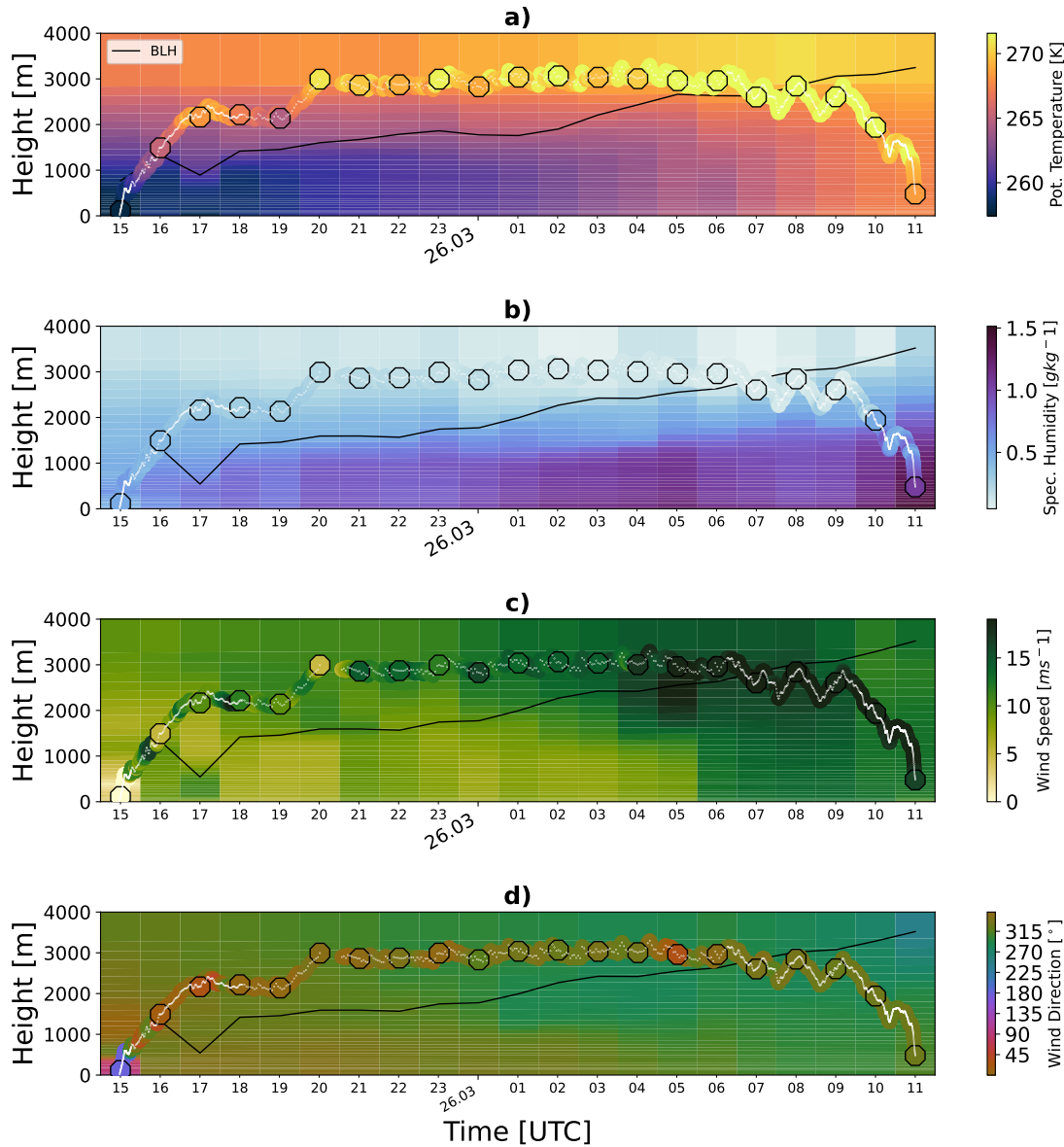
Figure 5.10: Time integrated vertical cross sections of different variables: a) potential temperature (K), b) specific humidity (gkg^{-1}), c) wind speed (ms^{-1}), and d) wind direction (°) from flight 2, with continuously updated AROME-Arctic forecast background. The flight path (white line) and the model evaluated positions (black circles) are highlighted. The black circles are also indicated every hour to keep track of the balloon's altitude. Simulated boundary layer height (BLH) is shown by the black line.

Fig. 5.10 reveals relatively good model alignment with the CMET, but also a few relatively outstanding differences. Again, a temporal increase in potential temperature and specific humidity from the surface layer building upwards with time is seen (Fig. 5.10a-b). Supporting the effects of strong surface turbulent heat fluxes destabilizing the boundary layer and mixing vertically upwards. Dryer and potentially warmer air is separated from this boundary layer by an inversion layer that is located on the sharp gradient in potential temperature and specific humidity. Notable is also how this mixed layer beneath is increasing with time in company with the deepening mixed layer. This is according to mCAO theory.

There is a relatively good correspondence between observations and AROME-Arctic overall. Best match seems to be obtained at the higher altitudes, where the CMET was floating at more or less the same height. On the other hand, less match is evident during the initial ascent and the early morning hours at the end of the flight, where potential temperature, indeed, appears gradually more amplified compared to the model (Fig. 5.10a). Wind speed, however, is more different (Fig. 5.10c). AROME-Arctic produces what appears to be a lower level jet between 2000 and 3000 meters at 04-05 UTC with wind speeds approaching 20 ms^{-1}. This increased wind speed is also found by the CMET. Nevertheless, AROME-Arctic struggles to sustain the strengthened wind speed over time, and as result, AROME-Arctic underestimated wind speed at the latest stage of the flight. Wind direction though, appears to be well reproduced (Fig. 5.10d). Wind direction is by the model estimated to initially be northerly, and gradually turning more north westerly. This direction modification does in fact not break through so clearly according to the CMET.

As per the previous CMET flight 4, the cross-section for CMET flight 2 has also been looked into to quantify model performance. Also this time including an updated (Latest time), and a non-updated (Initial time) forecast, which are shown in Fig. 5.11.
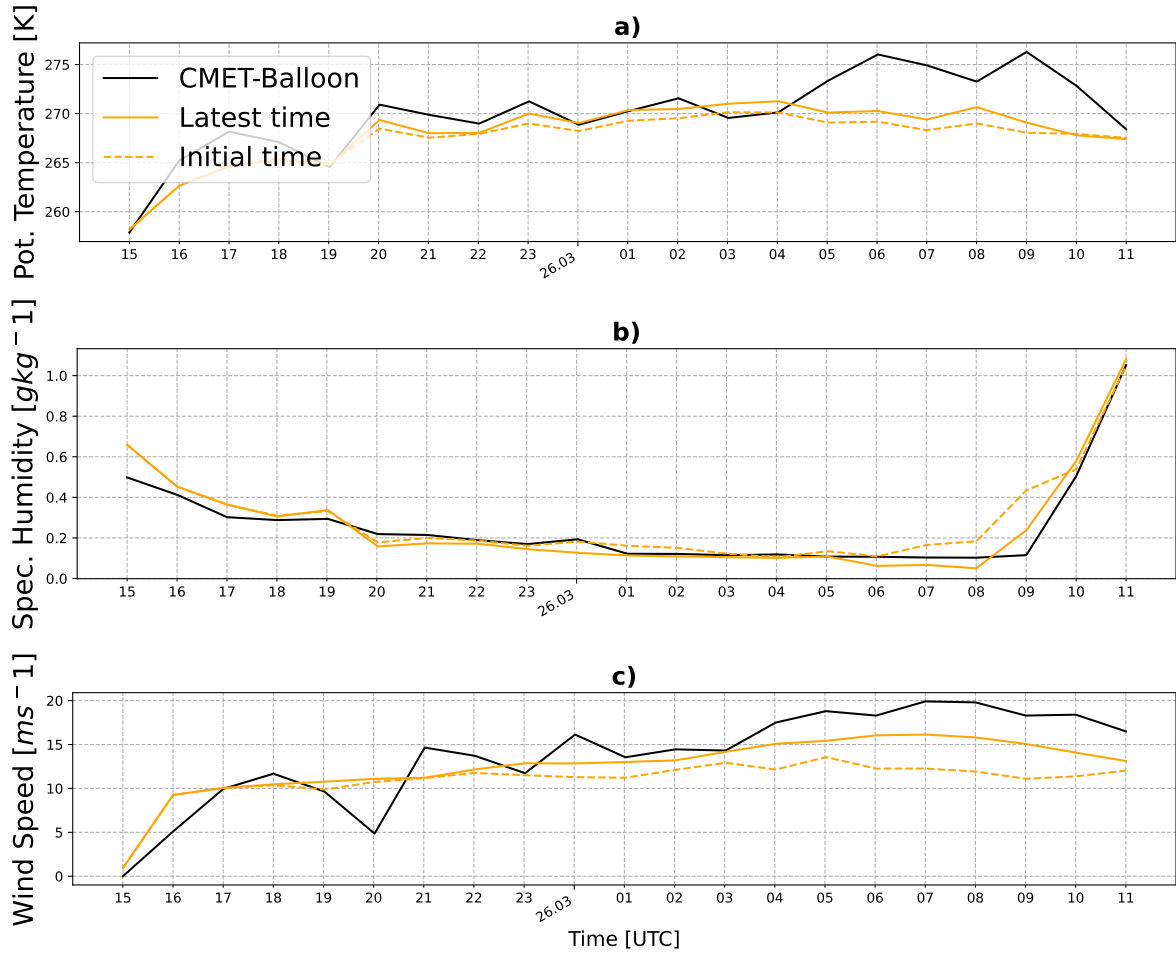
Figure 5.11: Time series of: a) potential temperature (K), b) specific humidity (gkg^{-1}), and c) wind speed (ms^{-1}) for the CMET 2 flight and AROME-Arctic forecasts issued at Initial time: 25.03.2022: 12 UTC (dashed orange line), and at Latest time: 25.03.2022: 12, 18, as well as 26.03.2022: 00, 06 UTC (solid orange line) for the nearest grid cell. CMET observations are indicated by the black line.

Tantamount to CMET flight 4, there is predominantly good correspondence between CMET and AROME-Arctic. Still, enhanced potential temperature remains evident, and a limited amount of variability exists between Initial time and Latest time (Fig. 5.11a). Similar can be said about the forecast variability with regard to specific humidity, which comes forward as slightly underestimated by AROME-Arctic (Fig. 5.11b). Nonetheless, the perhaps most outstanding difference between CMET and AROME-Arctic is found in potential temperature and wind speed (Fig. 5.11a,c). The observed increase in wind speed experienced by the CMET is not prevalent in neither of the forecast modes. Therefore, a pronounced gap between the CMET and the two investigated forecasts develops approximately after 03 UTC. Despite the misrepresentation, the Latest time managed to slightly improve the wind speed, although not entirely repairing the offset. Summary of mean, bias and root mean square error for the Initial time and Latest time with CMET flight 2 are depicted in Table 5.3.

Table 5.3: Mean, bias and root mean square error values for temperature and specific humidity from CMET and AROME-Arctic latest forecast along CMET 2-flight track.

	Potential temperature (K)		Specific humidity (gkg^{-1})		Wind speed (ms^{-1})	
	Initial	Latest	Initial	Latest	Initial	Latest
Mean	267.38	267.99	0.29	0.26	10.95	12.51
Bias	-2.58	-1.98	0.04	0.01	-2.73	-1.17
RMSE	3.55	3.05	0.09	0.06	4.58	2.94

AROME-Arctic again induces a negative bias for potential temperature (Table 5.3). The bias improves from -2.58 K on Initial time to -1.98 K on Latest time. A positive bias is present for humidity with 0.04 gkg^{-1} and 0.01 gkg^{-1} on Initial time and Latest time respectively. Wind speed appears under-predicted, which was suspected from Fig. 5.11. A tendency of decreasing bias amid the forecasts is seen in all parameters, indicating higher model confidence. RMSE displays increasing potential temperature, small reduction in humidity, and pronounced increase for wind speed.

5.4 FLEXPART simulations

The CMET 2 flight was to a large extent quasi Lagrangian. The CMET 2 flight was relatively long, and since the balloon found itself on an approximately constant height throughout the flight, it can be assumed to be partly representable for air mass transport. For this reason, it was decided to carry out simulations with the Lagrangian particle dispersion model FLEXPART. The goal was to simulate the pathway of the same air mass that the CMET balloon found itself in, and eventually, find a model trajectory that could be verified with the CMET trajectory. More specifically, FLEXPART-AROME, which in this case incorporates 3 dimensional wind from AROME-Arctic was utilized to simulate the spread of the computational air particles. Three runs were conducted (Table 3.6). In the following section, an analysis of two of the conducted simulations is presented, which includes the particle spread, trajectory analysis and a measure of the associated uncertainties.

5.4.1 First simulation

Results from the first simulation are displayed in Fig. 5.12. The first simulation contains the spread of 250 000 passive tracers released from a grid point at 3000 m, which corresponds to the position of the CMET balloon at 20:01 UTC. Fig. 5.12 figure shows a vertically integrated mass concentration of all the computational particles per grid cell volume. The dispersion is shown at four time steps starting from 4 hours after release, with 3 hours difference.
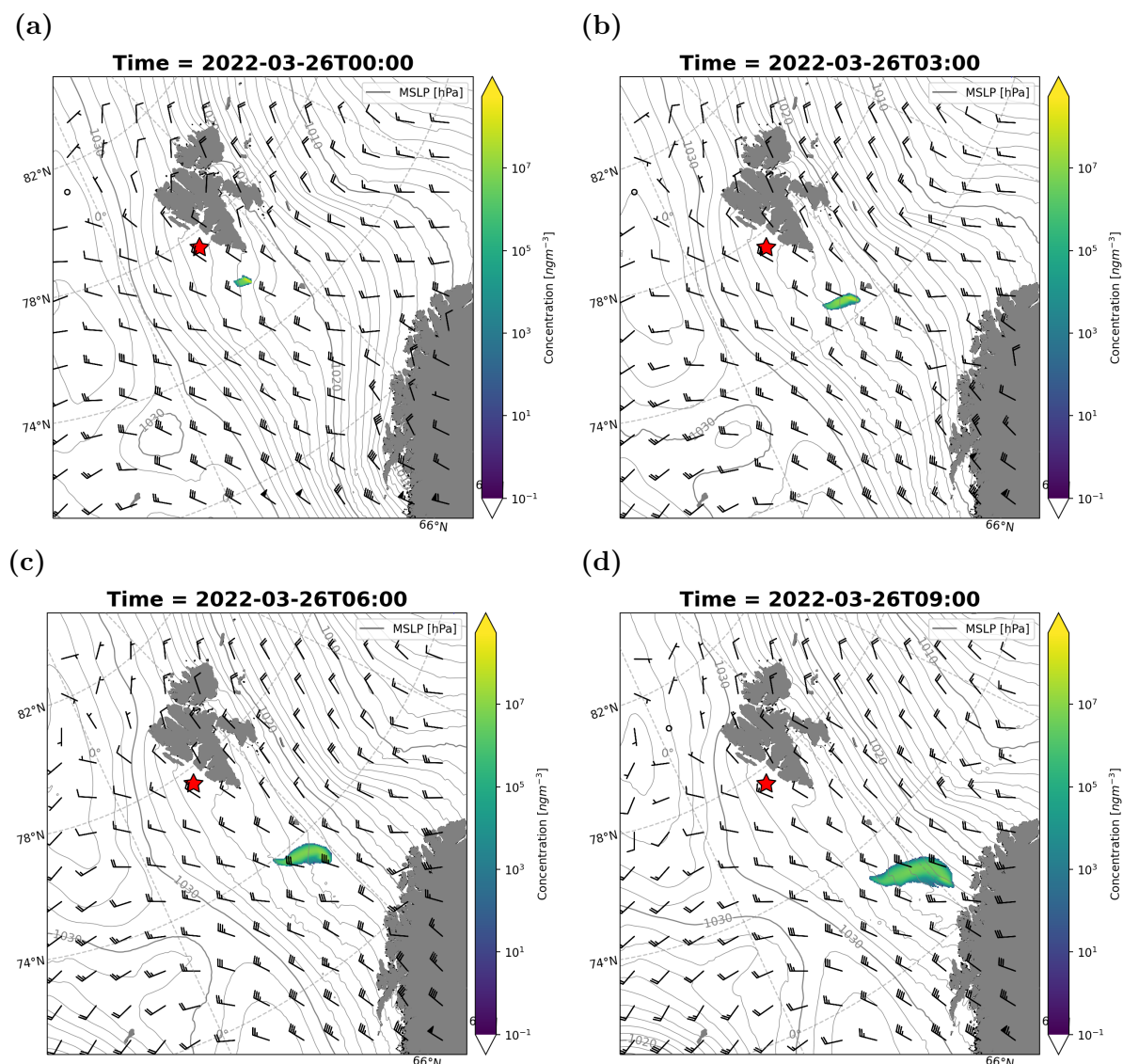
Figure 5.12: Volume concentration of the computational particles in nanograms per cubic metre valid for 26 March at: a) 00 UTC, b) 03 UTC, c) 06 UTC, and d) 09 UTC, including predicted mean sea level pressure (MSLP) in hPa and winds at 3000 m altitude from forecast initiated at 25.03.2022 18 UTC, similar to the applied simulation input field. The red star marks the location of particle release.

A distinct plume of high concentration can be identified (Fig. 5.12). The plume can be seen moving in a south easterly direction with time. The cover are of the plume increases with time, suggesting active horizontal spread of particles. The plume's horizontal shape varies from circular to rectangular, before it incorporates a more bow shaped structure in the direction of movement, which possibly could indicate a wind shear in the background flow. Contrary to the balloon, the particles were also allowed to move vertically. Below follows the mass concentration on the different vertical levels (Fig 5.13). The concentration is integrated over all latitudes and longitudes.
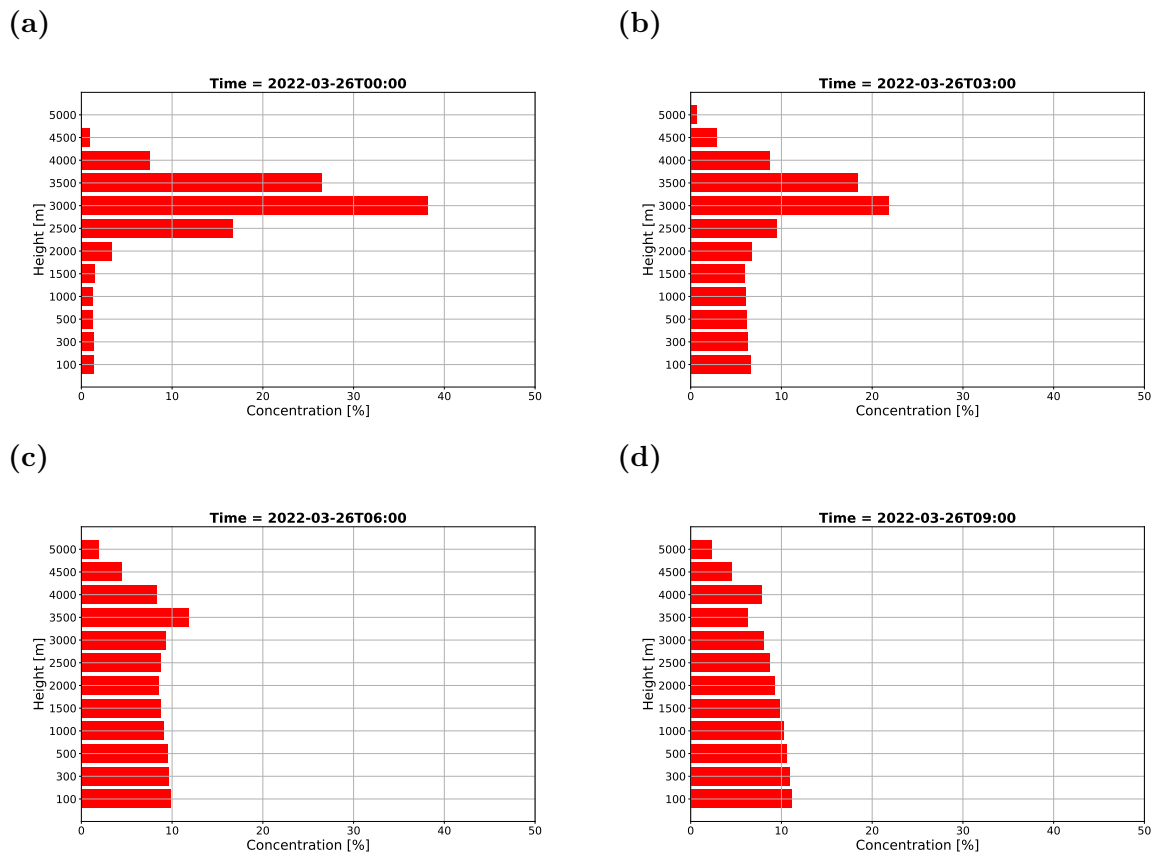
(a)

(b)

(c)

(d)

Figure 5.13: Longitude and latitude integrated vertical concentration distribution of the tracers in % at four time steps: 00 (a), 03 (b), 06 (c), and 09 (d) UTC.

Four hours after release (Fig. 5.13a), the majority of mass is at the 3000 m release height. However, one can observe that a great amount of particles have spread to 2500 m and 3500 m. Subsequently, more and more mass is put on the other model heights closest to the surface, as the plume gradually mixes. At 09 UTC (Fig. 5.13d), a pattern where concentration decreases with height is seen, and none of the model levels have more than 10% of the released particles, indicating that concentration is accumulated at the surface.

5.4.2 Trajectory comparison

A comparison with the CMET balloon has been carried out by the use of statistical methods. Due to considerable dispersion, a volume concentration based weighted mean of the plume's longitude and latitude has been calculated for every time step. The results are then used to construct an intended model trajectory that represents the movement of an air parcel. Fig. 5.14 shows the trajectory of the plume's weighted mean at 3000 m altitude, and 1 weighted standard deviation around the weighted mean. The trajectory of the CMET balloon is also shown for comparison.
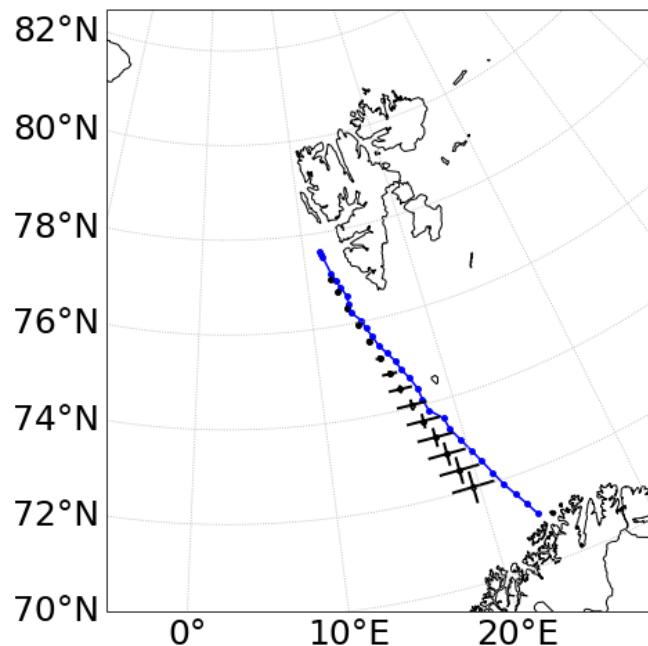
Figure 5.14: The time integrated horizontal distribution of particles at 3000 m height showing the weighted mean (black dots), ± 1 weighted standard around the weighted mean (crosses), the CMET balloon trajectory (blue line).

The CMET-balloon appears to be in close resemblance to the computed FLEXPART trajectory. However, it is evident the FLEXPART trajectory also gradually diverges from the balloon path. First, the model trajectory, even if it is hardly noticeable, drifts faster southward than what the balloon does. This head start is regained by the balloon a few hours later, as it is more obvious from Fig. 5.14 that the distance between the points decreases in the model trajectory, while the opposite happens for the balloon path. At the same time, the balloon starts drifting further east, and the uncertainty of the model trajectory increases. First, the trajectory uncertainty is linked to the modeled particles' longitudinal position, but on the later stages the model trajectory becomes less accurate both in terms of longitude and latitude, seen by the increasing cross size along the trajectory.

This suggests that the balloon was subjected to winds that were more westerly than anticipated by AROME. In addition, the enlarged uncertainty in parcel position could be a symptom of localized wind shears. Concerning the above mentioned errors in trajectory outcomes, it is beneficial to try to understand exactly when and where the trajectory errors appear. Finding the absolute horizontal transport deviation (AHTD) is one suitable method to determine this (Eq. 3.18, 3.19, 3.20). AHTD evaluates the horizontal distance between two different trajectories, and could give reliable information on trajectory errors.

5.4.3   Investigation of different heights

In addition, the CMET balloon did not fly completely at 3000 m height, but encountered minor height variations. Thus, to uncover how sensitive the modeled trajectory is to any vertical wind shear, an emphasis was put into evaluating two additional trajectories at 2500 m and 3500 m. In Fig. 5.15, AHTD for calculated FLEXPART trajectories at 2500 m, 3000 m and 3500 m are plotted versus time. AHTD was only evaluated until 09 UTC for the simulations, due the descent of the CMET balloon to lower altitudes after this time.
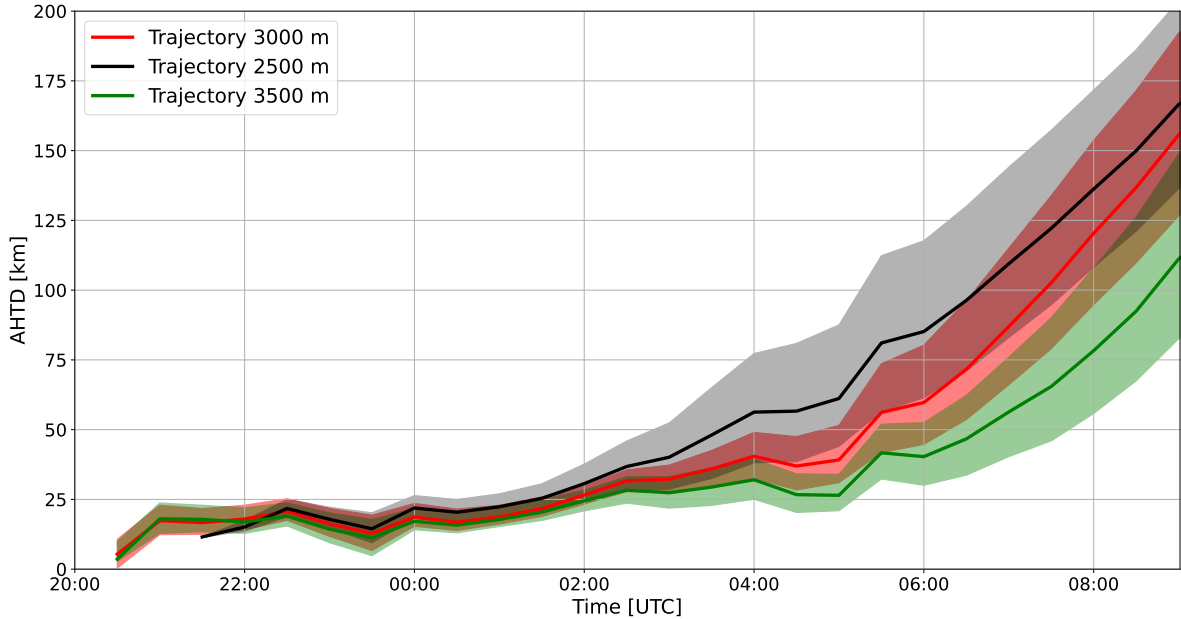

Figure 5.15: Time series of horizontal transport deviation (AHTD) in km between the CMET balloon and the weighted mean trajectories at 3000 m (red), 2500 m (black), 3500 m (green), and ± 1 weighted standard deviation around the weighted mean (shaded) for the firs simulation.

All model trajectories are within 50 km range from the CMET balloon 7 hours after release (Fig. 5.15). At 03:00 UTC, however, increasing AHTD is noticeable on all heights, where the lowermost at 2500 m increases faster compared to the 3000 m and the 3500 m trajectory, unveiling a general decrease in AHTD with height. The mean AHTD for 2500 m, 3000 m and 3500 m were found to be 55.7, 42.4 and 31.5 km respectively (Table 5.4). Despite that, all trajectory errors appear to grow exponentially when severe growth is first encountered. The difference in errors between 1000 m height grows to approximately 50 km during the end of simulation, which suggests the presence of a vertical wind shear. The relative horizontal transport deviation (RHTD), which is the percentage change in AHTD was also looked at for distinguishing how much the error grows for every time step (Fig. 5.16).
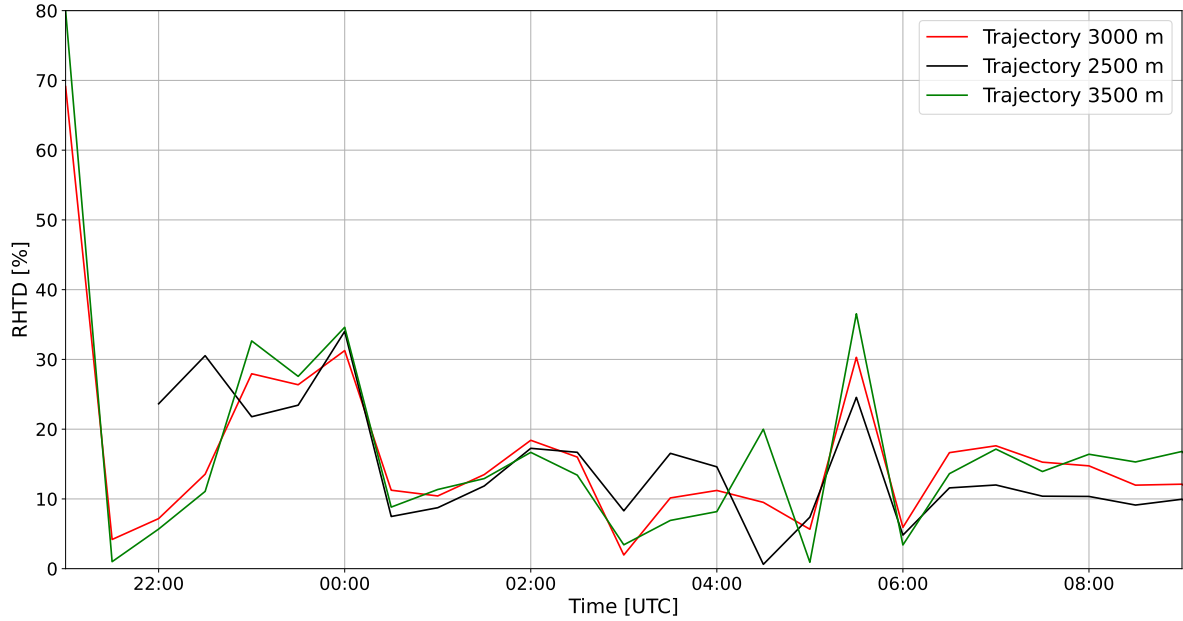
Figure 5.16: Time series of relative horizontal transport deviation (RHTD) in % between the CMET 2 balloon and the calculated trajectories at 3000 m (red), 2500 m (black), and 3500 m (green) for the first simulation.

The 3000 m, and 2500 m trajectories possess high RHTD right after release. After 22 UTC, the trajectories follow a similar pattern and are mostly below 30%. The RHTD also remains relatively constant with time for all heights, and there is not an increasing trend like what was seen in Fig. 5.15. Nevertheless, sudden spikes are appearing in the time series (00 UTC, 05:30 UTC) for all investigated heights. However, the trajectories also occasionally have different RHTD values (03-04 UTC) and (06-09 UTC). RHTD is more constant after 06 UTC, with values from 10% (2500 m) to 15% (3000 m, 3500 m), coinciding with the period where GPS signal was stable (Appendix B, Fig. B.3.)

5.4.4   Second simulation

For a further investigation into the period where the trajectories in Fig. 5.15 started diverging, a second simulation was run. In this simulation the same amount of particles were released 7 hours later (03 UTC) than the first simulation, and with forecast input initialized at 26.03.2022 00 UTC. The release location was picked based on the CMET balloon's position at 03 UTC, and the same calculation methods were carried out here. AHTD and RHTD from the second simulation are presented in the following (Figs. 5.17, 5.18).
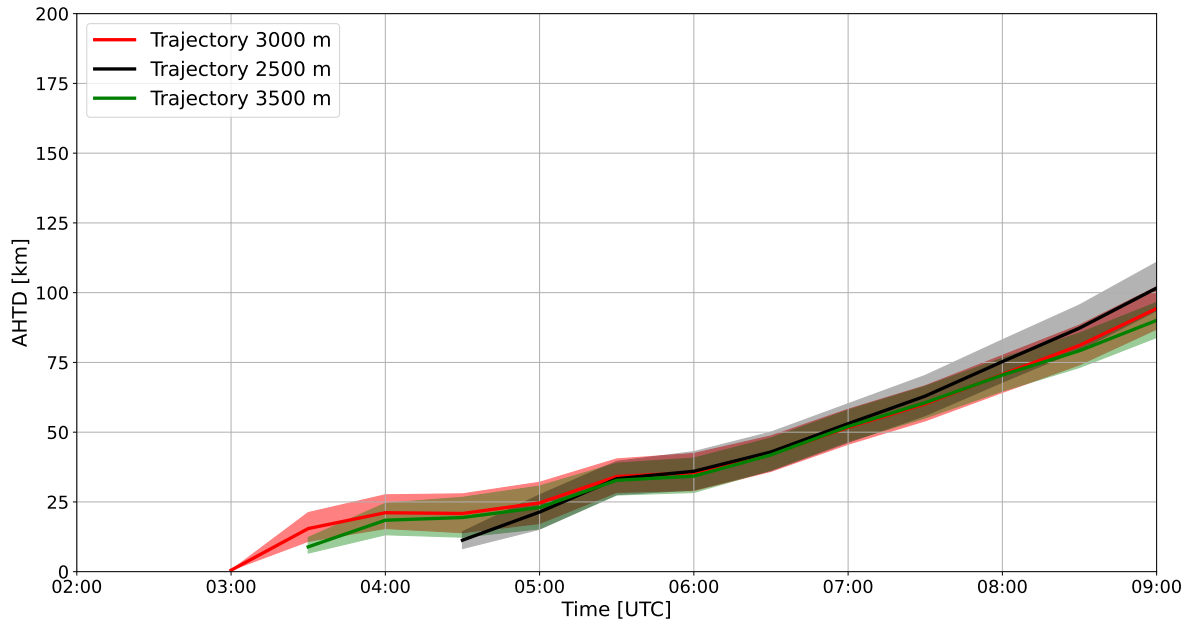
Figure 5.17: Time series of horizontal transport deviation (AHTD) in km between the CMET balloon and the weighted mean trajectories at 3000 m (red), 2500 m (black), 3500 m (green), and $\pm$ 1 weighted standard deviation around the weighted mean (shaded) for the second simulation.

There is generally good agreement between the different trajectories. Similar to the first simulation (Fig. 5.15), the displayed time series are cut off at 09 UTC. It can be noticed that the 3000 m trajectory starts at 0 km at 03 UTC (Fig. 5.17) which differs from the first simulation (Fig. 5.15). This is a result of the release time and that 30 min output data of average concentrations are retrieved in the simulations. The spreading of particles goes faster upward than downward, and could also be seen in Fig. 5.15. At the same time, the AHTD remains below 100 km for the entirety of the shown time. However, the 3000 m trajectory spends 6 hours reaching approximately 100 km, while for the first simulation it took 11 hours (Fig. 5.15). Nevertheless, the total AHTD was reduced compared to simulation 1, with mean AHTD values of 42, 34.4 and 36.2 km for the investigated heights (Table 5.4). Like in the first simulation, the RHTD was also looked into here and is shown below (Fig. 5.18).
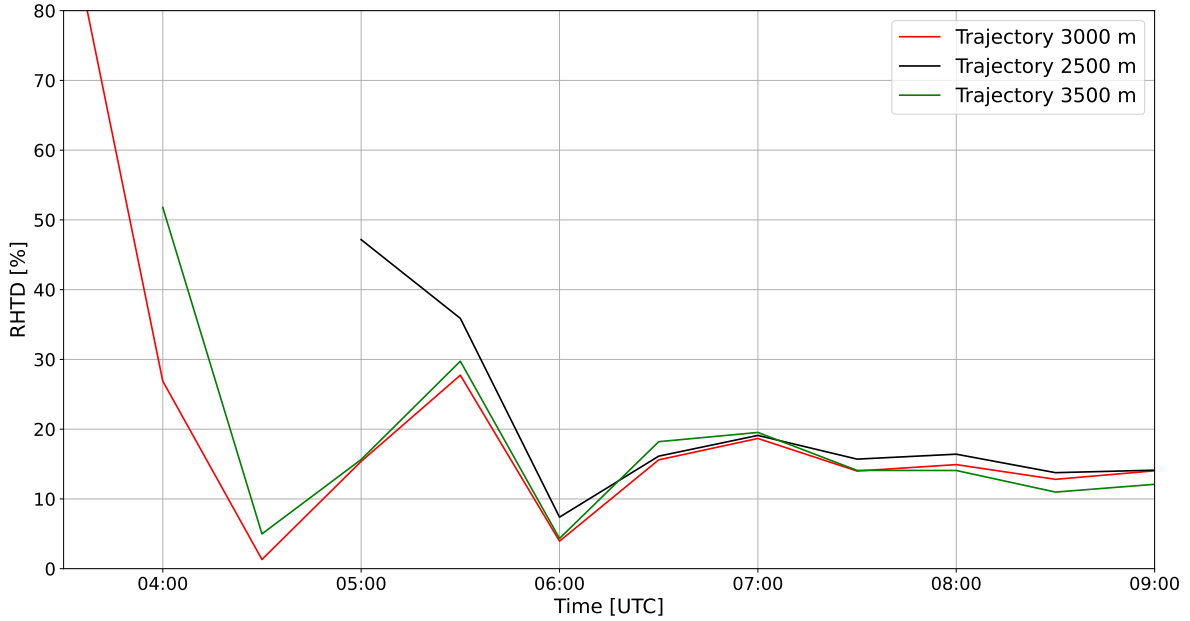
Figure 5.18: Time series of relative horizontal transport deviation (RHTD) in % between the CMET 2 balloon and the calculated trajectories at 3000 m (red), 2500 m (black), and 3500 m (green) for the second simulation.

The previously mentioned spikes are also seen here (Fig. 5.18). Again, there are also high values at the beginning of the simulation, which is a result of the calculation procedure for RHTD. Simulation 2 is also compared to the CMET in a shorter time period, compared to simulation 1, and is probably explaining the higher RHTD values encountered here ranging from 18.3 to 22.5 %. The mean AHTD and RHTD for all the calculated FLEXPART trajectories from simulation 1 and 2 are shown in Table 5.4.

Table 5.4: Mean AHTD (km) and RHTD (%) for the calculated trajectories at 2500 m, 3000 m, 3500 m from the two investigated simulations.

	AHTD (km)			RHTD(%)		
	2500 m	3000 m	3500 m	2500 m	3000 m	3500 m
Simulation 1	55.7	42.4	31.5	14.8	16.7	17.2
Simulation 2	42.0	34.3	36.2	21.4	22.5	18.3

6. Discussion

In the following section an assessment of the retrieved results is presented. The results will be evaluated in context of the two research questions: 1) To what extent are the results trustworthy, what are the limitations? 2) How reliable are the retrieved CMET data in obtaining useful information on air mass transformation in mCAOs? An overview of various limitations will be discussed.

6.1   CMET compared to AROME-Arctic

Both investigated CMET flights showed good agreement with AROME-Arctic. Increased boundary layer temperature and humidity with time was observed along the flight paths, which was also generally well reproduced by AROME-Arctic. The AROME-Arctic model represented mesoscale features such as inversions, lower level jets and increasing boundary layer height which also were recorded by the two investigated CMET flights. This suggests CMET balloons are able to provide reliable data on the transformation of a moving air mass. Nevertheless, the spatial and temporal distribution of some of the model features seem to occasionally differ from the CMET observations.

The highest mean potential temperature was recorded on flight 4. Nevertheless, AROME-Arctic underestimated potential temperature on both flights, with flight 2 experiencing the largest bias and RMSE. On the other hand, AROME-Arctic overestimated specific humidity for both flights, with substantially higher values for flight 4 than flight 2. With regard to wind speed, the trend was more unclear. Too high wind speed was predicted for flight 4, but for flight 2 the predicted wind speed was too low compared to the observations. There are different factors that can explain the discrepancies.

6.1.1   Uncertainties in the CMET data

Uncertainty in the CMET data could be an important explanation. Investigation of all the CMET balloon profiles with the nearest radiosonde profiles in Ny-Ålesund revealed that the CMET balloons encountered slightly enlarged potential temperature and wind speed, plus reduced specific humidity compared to the radiosondes. This finding was reinforced by the similar tendency in the launch profile from flight 2. This suggests that the CMET measurements could be slightly too warm and dry compared to radiosonde measurements, and that should be brought in mind when interpreting the results. Another important factor here is that the radiosondes are not entirely independent from the model data, as the radiosondes also are used in the model assimilation (Müller et al., 2017a). The minor differences between CMET and radiosondes could possibly have originated from either i) Enhanced heating experienced by the CMET, or ii) Greater horizontal drift on the CMET balloons.

First, the higher temperature and reduced humidity might have come as a result of an extra heating effect from the boundary layer around the CMET balloon. This element was discussed in (Dale et. al, 2020), who found that hysteresis, which is the build up of a heated pocket of air around the balloon, was observed. In particular during ascent, and that this effect was partly inevitable despite the fact that the instruments were sitting on a 800 mm boom pointing out from the balloon to reduce the impact of the heating.

Second, the offset could be explained by the drift in balloon trajectories. The CMET and radiosonde are compared to a vertical profile from AROME-Arctic that only describes one grid point in the model, while the balloons are allowed to drift horizontally during the ascent. Additionally, the CMET might also drift for more than one hours until reaching the 2000 m height, and depending on the wind speed, the CMET balloon might have diverted far away from Ny-Ålesund. Consequently, the CMET balloon could have encountered new air masses, as this coastal region might arrange extensive local mixing of marine and land based air masses (Roberts et al., 2016). This could make profile comparison questionable, and could explain the increasing differences with height. Simultaneously, a similar tendency was also found in the difference from the radiosonde, that requires a much less spatio-temporal cover area than the CMET balloon. Subsequently, this proposes an offset in model performance between the surface and upper air.

As mentioned, the scale of the modeled features by AROME-Arctic appear different in size compared to observed CMET data. On flight 2, a lower level jet was reproduced by the model, but the recorded wind speed appeared however, larger in scale. Moreover, during flight 4, a narrow inversion was identified, although not as dry as prescribed by CMET. The observed inaccuracies might not be related to the ability of AROME-Arctic to resolve mesoscale atmospheric processes, but rather a result of the representativeness of the observations. The lack of GPS signal represents a considerable limitation with this study. The mean difference between the iridium and GPS coordinates during all flights was found to be in the range of 200-1000 m. Even if the difference between GPS and Iridium were not considerably high, it might occasionally have convinced the model to pick the wrong model grid point during analysis. One would think that this has less consequences if dealing with a lower resolution global model, but for a high resolution model like AROME-Arctic, which probably has a higher likelihood of capturing smaller scale structures in high details, this could perhaps cause discrepancies with observations on relatively small distances. Therefore, the model data near shore should be treated with great caution (Roberts et al., 2016).

Another potential uncertainty from the GPS outage is the altitude parameter. The calculated hypsometric height is well suited for Ny-Ålesund, but on later stages of the flight, the air mass takes up heat and moisture, and the assigned height might be too low. Despite that, the hypsometric height does match the GPS height to such a satisfying degree that it was decided to stick with it, and not modify the height by applying more vertical profiles downstream. Although this height underestimation might be a reason behind the temporary increased bias in potential temperature in flight 2. Nevertheless, this might also have physical explanations such as solar exposure or boundary layer entrainment. Entrainment of warmer air from the convective boundary layer could have been mixed upwards with free troposphere just above, and consequently enhanced the temperature.

6.1.2   Changes with different lead times

Inspection of the Initial and Latest time forecasts also exposed differences. The mean potential temperature and specific humidity increased from the Initial to the Latest time during flight 4, while the wind speed decreased. In flight 2, there was also an increase in potential temperature, but decreasing specific humidity, and at the same time increasing

wind speed. AROME-Arctic performance was improved by reduced bias and RMSE between the Initial and the Latest time forecasts in both flights, except for specific humidity during flight 4. The different model runs could be interpreted in the sense of predictability. The results suggest that there was a greater amount of uncertainty related to the forecast during flight 4 then flight 2. The low wind speed and mixing of air masses originating from different source regions near the sea ice edge close to the balloon path could have influenced the results and increased uncertainties.

The potential temperature RMSE from flight 2 and flight 4 lie within the range of RMSE values that was reported by Dale et al. (2020), where RMSE was found to be from 1.23 to 4.05 K. For this study it was found to be between 2.38 and 3.55 K. The results suggest that CMET balloons were fully functional also in a mCAO conditions. At the same time, Dale et al. (2020) also reported increased RMSE during the forecast periods of one of the CMET flights, and noted that the particular CMET stopped profiling underway, which Dale et al. (2020) argued could have an effect on the results. It is also noteworthy in this case that AROME-Arctic performed better against the CMET 4 flight, with RMSE of 2 K, a flight that had multiple vertical profiles, than compared to CMET 2 that did not carry out vertical profiles underway, consequently causing RMSE of above 3 K. As a result of this, CMET 2 flight might have suffered from too low ventilation because of too low vertical velocities, and therefore the recorded temperature was artificially enhanced. The filtered data from the quality tests, however, were not considered in this study. Possibly would the RMSE values for flight 2 have been improved if some of the filtered data points were ignored. At the same time, both specific humidity and wind speed were below all RMSE values from Dale et al. (2020). However, the investigated data is only at hourly resolution. This means that there is reduced knowledge on time scales below 1 hour. The balloon might cross 10-20 model grid points between every evaluated grid point. Evaluation of the variability within 1 hour was looked into for flight 4, but larger variations were not found for that particular case (Appendix C, Figs. C.1, C.2).

6.2   CMET compared to FLEXPART-AROME

The calculated trajectories follow the pathway of CMET flight 2 to a reasonable extent. An investigation of 3 different vertical levels revealed that calculated trajectories on 2500 m, 3000 m and 3500 m encountered different values of AHTD. The lowest AHTD in simulation 1 was found on the 3500 m height with a mean AHTD of 31.5 km, while in simulation 2, the lowest mean AHTD was found on the 3000 m height with a mean value of 34.2 km. However, in both simulations, the highest AHTD was encountered on the 2500 m trajectory. The mean RHTD values were found to be 14.8%-17.2% for simulation 1, and 18.3%-22.5% for simulation 2.

The results showcase that CMET balloons provide reliable data for transport modeling in mCAO conditions. The RHTD results are significantly lower compared to the RHTD results reported by Riddle et al. (2006), who reported RTHD values of 26% and 34%. But before drawing conclusions, a greater look must be put into the different limitations with the results.

6.2.1 Sources of trajectory error

First of all, one explanation of the improved RHTD could be related to the input model. For this study, the high resolution NWP model AROME-Arctic was utilized for wind field input. Riddle et al. (2006) on the other hand, utilized global models from ECMWF and GFS, which suggests that in their study the model representation of winds were less accurate, and that could have consequently led to larger trajectory errors. Nevertheless, this might also have a counteracting effect, as higher resolution might not improve the results significantly (Riddle et al., 2006).

Secondly, the reduced errors might be a result of the calculation method. One of the limitations with this study is that only one CMET flight has been compared with FLEX-PART, in contrast to Riddle et al. (2006) and Mentzoni (2011) who utilized several CMET flights. Consequently, there is substantially less flying time available, which reduces the quality of the results. There was an opportunity to compare more flights, but due to relatively short flights and numerous vertical soundings on most of the other CMET flights, it was decided to just compare CMET flight 2. Flight 2 was the only flight where the balloon flew at more or less the same altitude for a sufficient period of time.

One of the strengths with the study, however, is the trajectory calculation method. By calculating a weighted mean trajectory based on particle concentration, one is better able to account for the uncertainty in the particle trajectories. Subsequently, one would also think that the amount of released particles could impact the outcome of the calculated trajectories, especially if the amount of released particles is too low.

6.2.2 Investigation of a potential wind shear

To discover the driving mechanisms behind the spread in AHTD for simulation 1, a further investigation into NWP model output from AROME-Arctic was considered to explore potential wind shears. According to Riddle et al. (2006) there are three sources to trajectory errors. i) Truncation errors, ii) Wind field errors, and iii) Wind gradient errors. The truncation errors relate to the computation of the particle trajectories, while the wind field error relates to errors connected to the performance of the NWP input model. Nevertheless, what Riddle et al. (2006) pointed out as the most influential error source was the wind gradient error. Errors that relate to local scale wind effects such as lower level jets. When considering Fig. 6.1, which displays the horizontal and vertical wind speed along the 3000 m FLEXPART trajectory, one can notice an area of enhanced wind shears south of 73 °N. This finding strengthens the probability that the particles have been subjected to various wind speeds on the different altitudes during the simulation.

The vertical wind shear could possibly be related to the position of the boundary layer height (Fig. 6.2). Due to the decreasing AHTD with height it can be thought that the boundary layer height from AROME-Arctic was overestimated during the CMET flight. To dynamically explain the reasons behind this could be difficult. However, a possible explanation could be the presence of a reverse shear environment near the position of the CMET and the calculated FLEXPART trajectories. Such reverse shear environments appear on the right-hand flank of a cold air outbreak air mass as a result of the thermally driven wind direction acting in the opposite direction of the mean wind, and are often

characterized by a strong low level jet (Terpstra et al., 2016).

Ultimately, the trajectory errors encountered here are most likely originating from a combination of wind field errors and wind gradient errors. Based on the high wind speed bias (Fig. 5.11) collocated with the timing of growth in AHTD (Fig. 5.15) it means that wind field error must play an important role in explaining the encountered trajectory errors from the two simulations. However, judging from the position of localized lower level jets (Fig. 6.1) together with varying boundary layer heights (Fig. 6.2) there are clear indications that wind gradient errors could explain the trajectory errors as well.
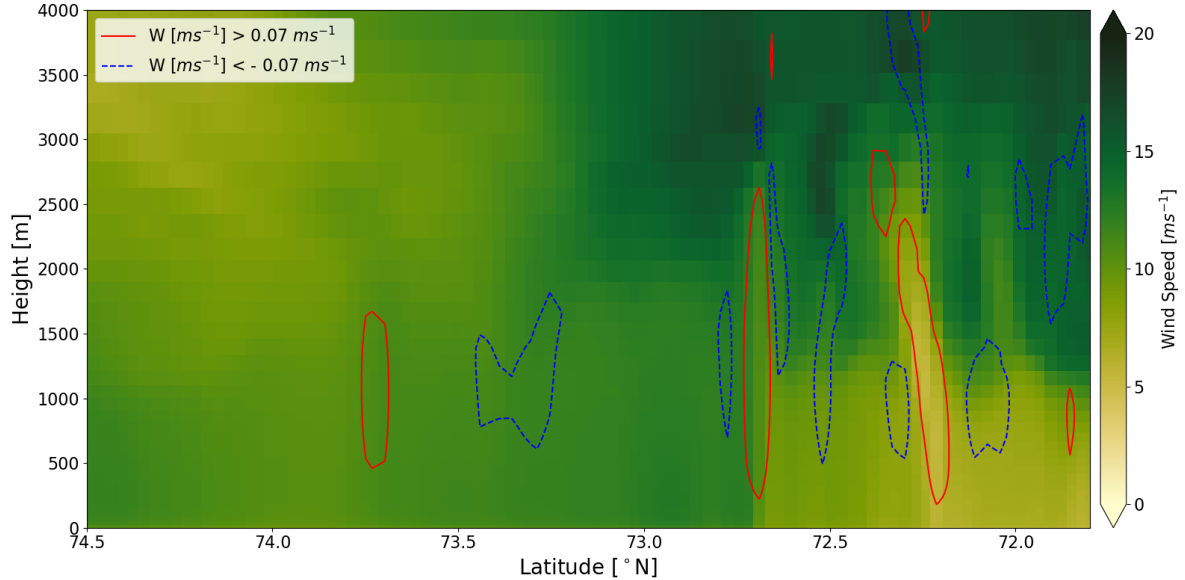

Figure 6.1: Vertical cross section between Bjørnøya and Norwegian main land displaying horizontal and vertical wind speeds (ms^{-1}) along the computed FLEXPART 3000 m trajectory from simulation 1. Forecast retrieved from 25.03.2022 18 UTC and valid for 26.03.2022 07 UTC.
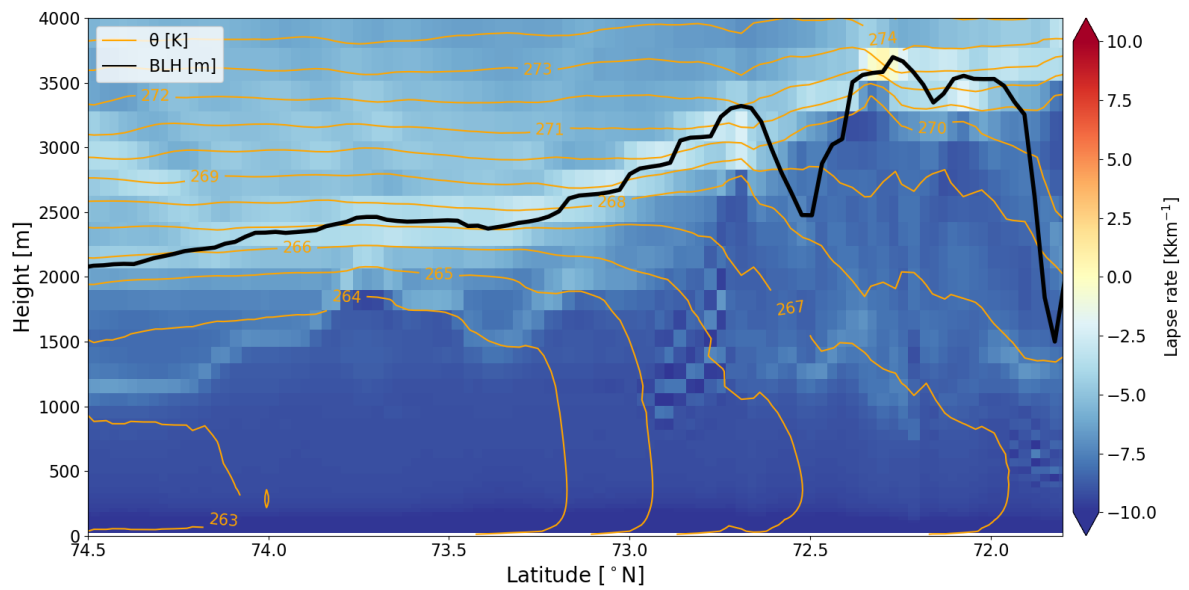
Figure 6.2: Vertical cross section between Bjørnøya and Norwegian main land showing temperature lapse rate (Kkm^{-1}), potential temperature θ (K), and boundary layer height (m) along the computed FLEXPART 3000 m trajectory from simulation 1. Forecast retrieved from 25.03.2022 18 UTC and valid for 26.03.2022 07 UTC.

7. Summary and conclusion

Observations from controlled meteorological (CMET) balloons during marine cold air outbreaks (mCAOs) in the Nordic Seas were studied to evaluate the quality of CMET balloons in providing useful data of Arctic air mass transformation. In total 6 CMET balloons were launched from Ny-Ålesund in the period 26 March-04 April 2022 in association with the ISLAS-2022 field campaign. The CMET flights conducted vertical profiles of the boundary layer and sampled drifting air masses. However, due to substantial GPS outages, the retrieved CMET data had to be processed in order to account for missing data. Coordinate gap filling, altitude and wind calculation were carried out in order to create a quality controlled CMET data set.

Results from two CMET balloons were then analyzed using data from radiosonde, dropsonde and model output from the operational NWP model AROME-Arctic with different lead times. Both CMET fights showed good correspondence with AROME-Arctic forecasts. Increasing boundary layer temperature and humidity were evident in the forecasts and represented in the CMET data. Flight 4 was found to have higher model accuracy than flight 2. On the other hand, flight 4 experienced the least improvement in forecast performance with decreasing lead time, and especially high variability was seen in the predicted humidity.

Furthermore, relatively large wind errors were found in flight 2. To reveal how this impacts the transport of air masses, simulations with the Lagrangian particle dispersion model FLEXPART-AROME were carried out. Two simulations with different forecast initializations and release locations were studied here. Calculated model trajectories of the released particles weighted mean were considered at three different altitudes in order to do comparison with the CMET flight trajectory from CMET flight 2. The mean AHTD and RHTD was found to be between 31.5 and 55.7 km, and 14.8 and 17.2 % for the first simulation, while for the second simulation it was found to be between 34.3 and 42 km, and 18.3 and 22.5 %.

Further analysis revealed that a vertical wind shear was present in the FLEXPART trajectory where the AHTD growth was encountered. This could explain the discrepancies seen between the trajectories at different heights. Overall, from this study, it was shown that the verification results from the comparison between CMET and AROME-Arctic and between CMET and FLEXPART are within the range of what has been reported by previous similar studies. The RHTD values were indeed found to be considerably lower than previous studies.

In conclusion, this study provides an unique analysis of CMET observations in mCAO conditions in a challenging Arctic environment. The study shows that CMET balloons provided useful data of Arctic air mass transformation during mCAOs. However, there are certain limitations with regard to GPS signals that cause uncertainties, especially for the calculated wind speed values. If one should focus on local scale wind measurements from CMET balloons, then it is a necessary criteria with stable GPS signal. However, for all the other parameters, the retrieved CMET data show good quality. The main finding from this study is that it is fully possible to retrieve useful data on air mass transformation from CMET balloons, even in a challenging Arctic environment.

Future work

For future work, one should try to apply filtered data to a larger extent in the analysis to see if there are notable differences in the results. One should also try to aim for more CMET flights during mCAOs, and find inventive ways to make the CMET balloons more resistant to icing, so that more data could be taken within clouds. In addition, it would have been useful to apply FLEXPART more actively in the planning stages of CMET flights, and aim for several CMET flights at different altitudes simultaneously to better investigate the impact of wind shear on air mass transport.

Appendices

A Balloon launces

Table A.1: Overview of all radiosonde launches from Ny-Ålesund and Bjørnøya during and 12 hours before and after every CMET balloon launch. Launches used for estimating the CMET altitude are marked by a (*) sign.

| Date	Ny-Ålesund (UTC)	Bjørnøya (UTC)	Dropsonde (UTC)	CMET (UTC)
24 Mar	11:02	11:10	-	-
24 Mar	16:46*	17:10	-	14:54
24 Mar	22:47	23:10	-	
25 Mar	04:49	05:10	-	-
25 Mar	10:47	11:10	-	-
25 Mar	16:52*	17:10	-	14:58
25 Mar	22:51	23:10	-	
28 Mar	16:59	17:10	-	-
28 Mar	22:50*	23:10	-	22:50
29 Mar	-	02:10	-	
29 Mar	04:52	05:10	-	
29 Mar	-	08:10	-	
29 Mar	10:57	11:10	-	
29 Mar	10:57	11:10	-	
29 Mar	-	14:10	-	
29 Mar	16:58	17:10	-	-
29 Mar	-	20:10	-	-
29 Mar	22:46	23:10	-	-
30 Mar	04:53*	05:10	-	02:14
30 Mar	10:53	11:10	13:06	
30 Mar	17:08	17:10	-	
30 Mar	22:46	23:10	-	
31 Mar	04:46	05:10	-	-
31 Mar	10:53	11:10	-	-
03 Apr	16:47	-	-	-
03 Apr	22:48	-	-	-
04 Apr	04:51*	-	-	02:06
04 Apr	10:54	-	-	
04 Apr	17:01	-	-	-
04 Apr	22:48	-	-	-

B GPS data
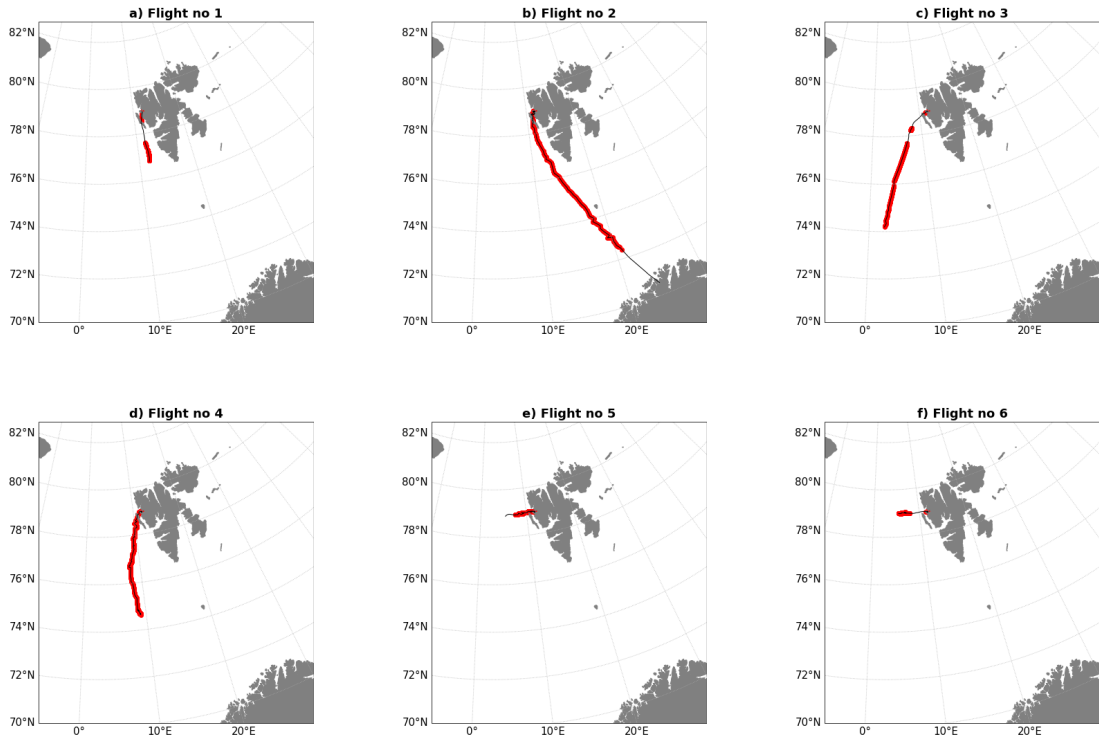
Figure B.1: Flight paths for CMET flight no 1 (a), 2 (b), 3 (c), 4 (d), 5 (e) and 6 (f) with areas of gps outages (red).
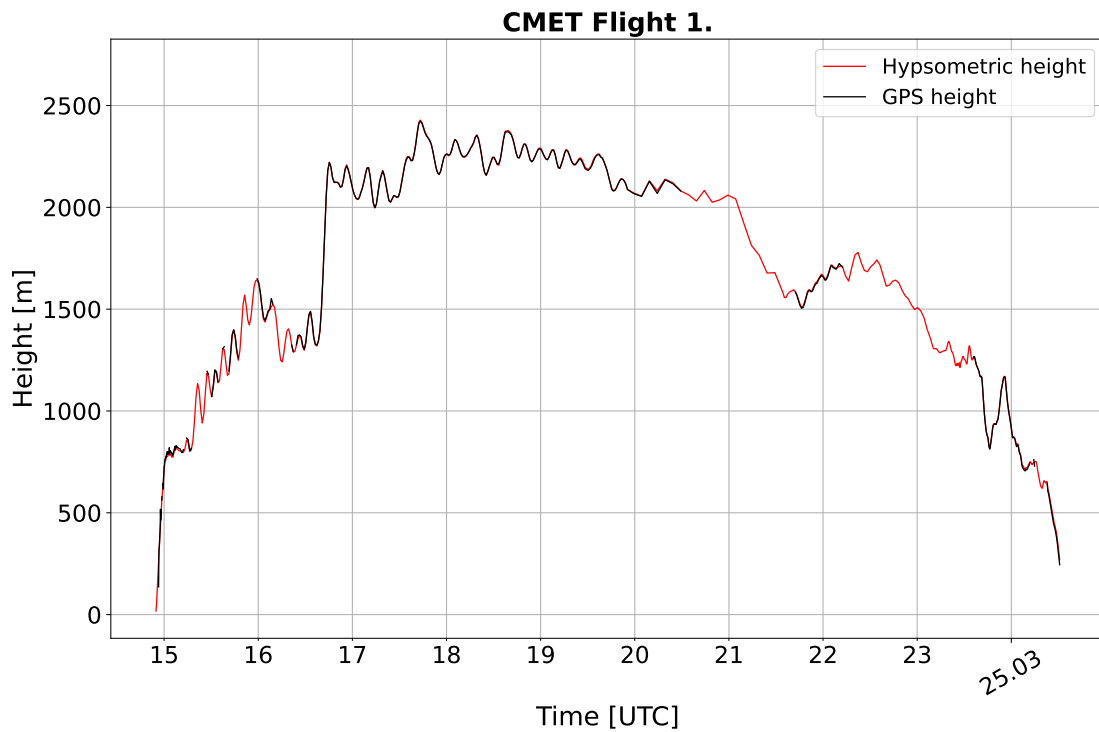

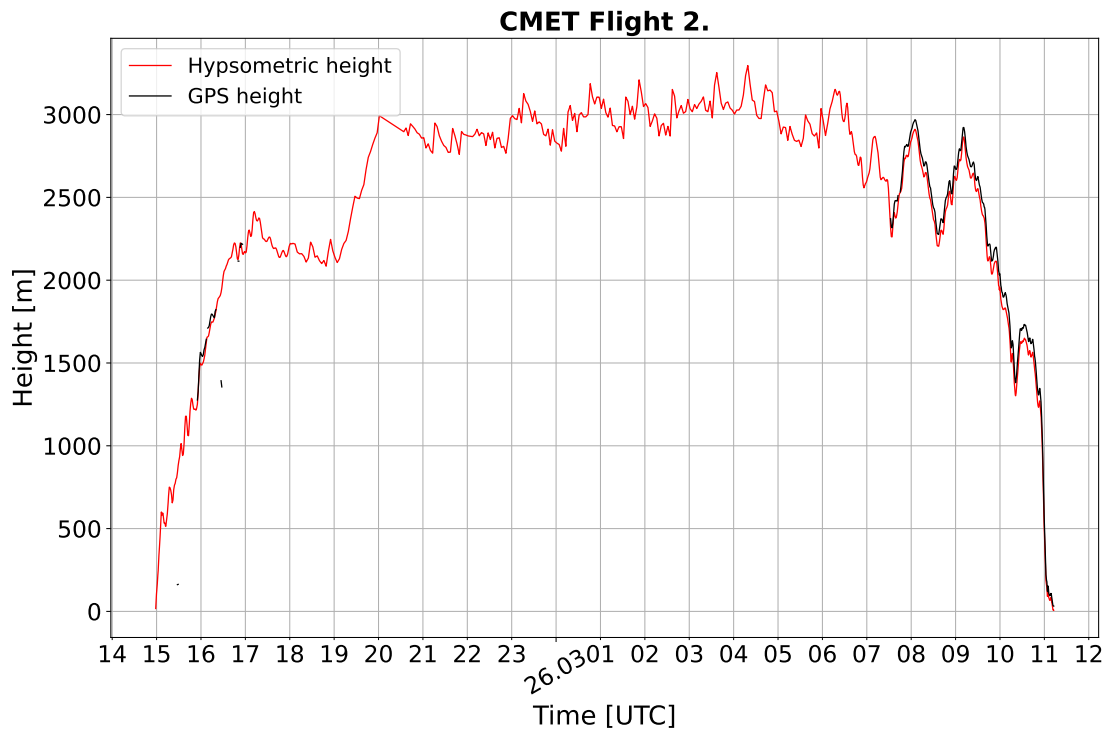**Figure B.2:** Calculated hypsometric height (red) and recorded GPS height (black) from CMET flight 1.

Figure B.3: Calculated hypsometric height (red) and recorded GPS height (black) from CMET flight 2.
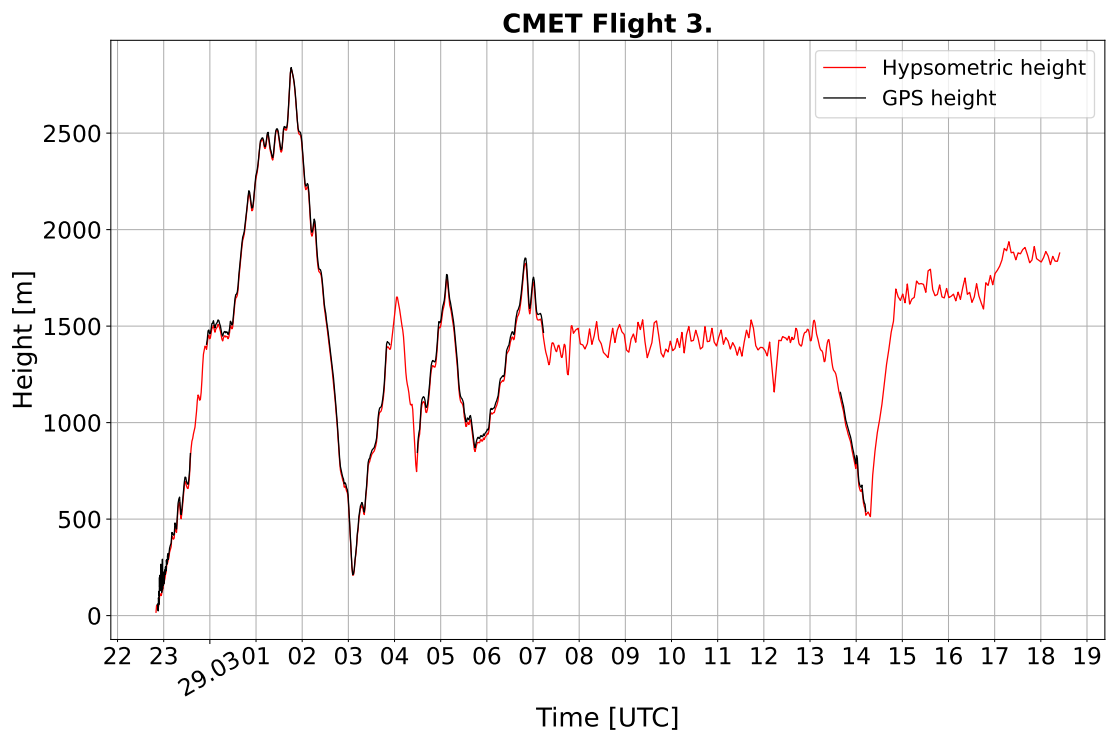

Figure B.4: Calculated hypsometric height (red) and recorded GPS height (black) from CMET flight 3.

Figure B.5: Calculated hypsometric height (red) and recorded GPS height (black) from CMET flight 4.

Figure B.6: Calculated hypsometric height (red) and recorded GPS height (black) from CMET flight 5.
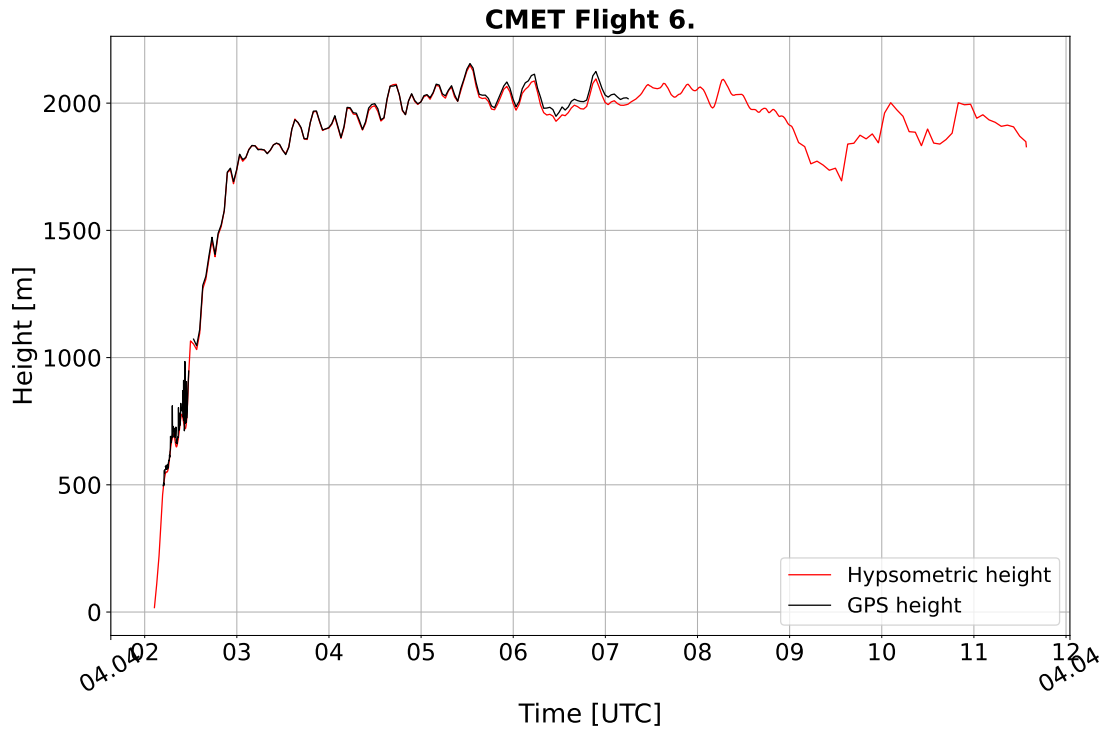
Figure B.7: Calculated hypsometric height (red) and recorded GPS height (black) from CMET flight 6.
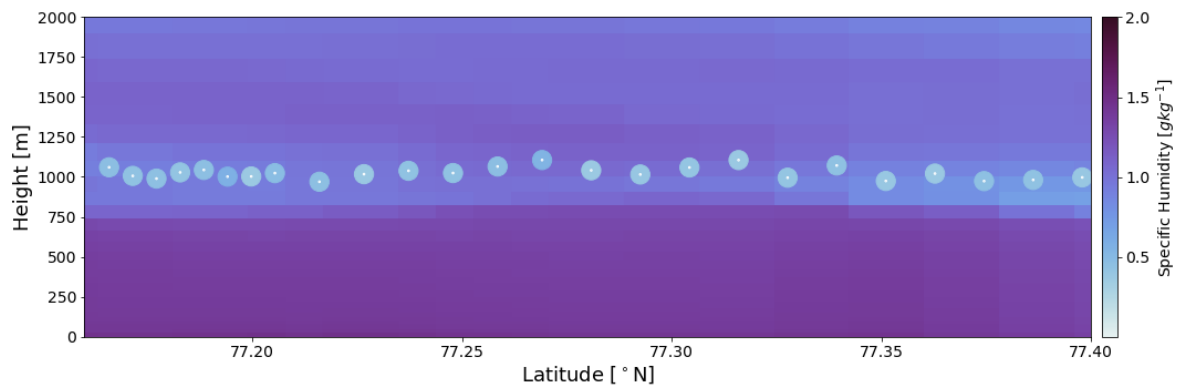
C Vertical cross sections

Figure C.1: Fixed time cross section of specific humidity (gkg^{-1}) for CMET balloon and AROME-Arctic background corresponding to measurements at 13-14 UTC on 30 Mar 2022 with forecast initiated at 30 Mar 2022 12 UTC.
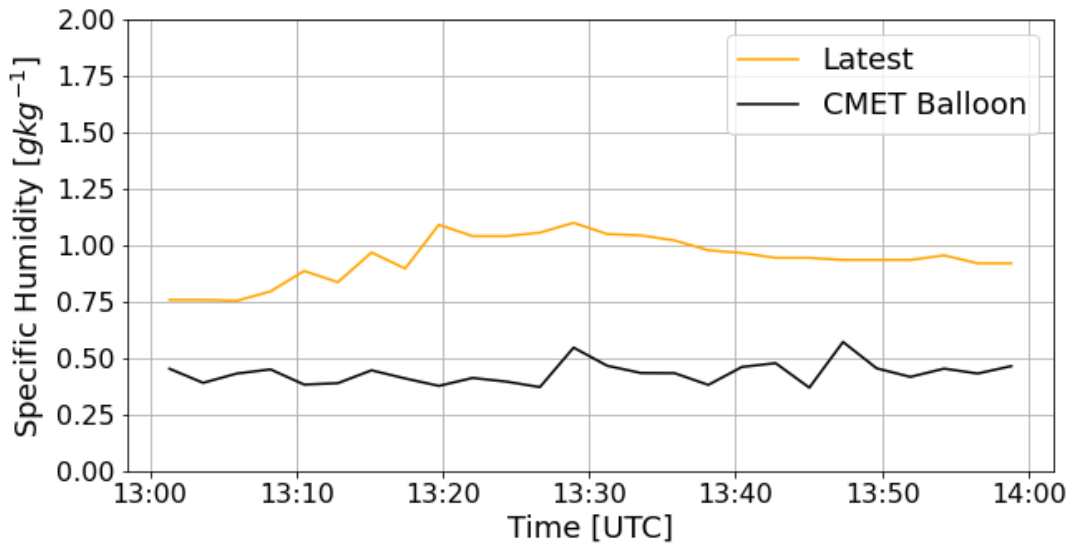
Figure C.2: Fixed time series of specific humidity (gkg^{-1}) for CMET balloon (black) and nearest AROME-Arctic grid point and model level (orange) at 13-14 UTC on 30 Mar 2022 with forecast initiated at 30 Mar 2022 12 UTC.
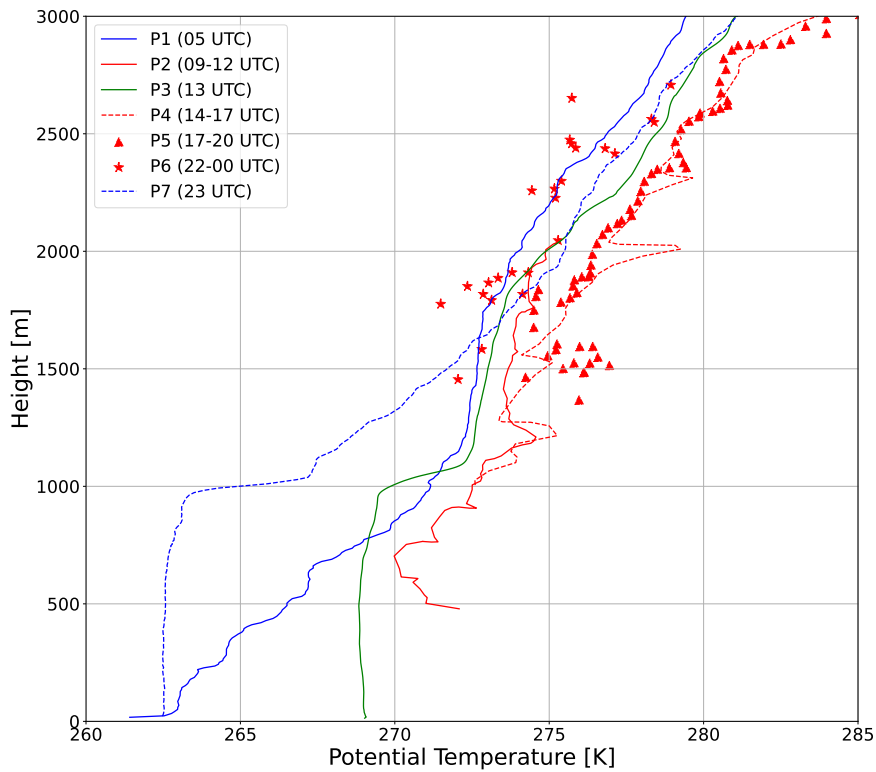

Figure C.3: Vertical profiles from 30 Mar 2022 of potential temperature from CMET balloon (P2, P4, P5, P6) (red), radiosondes (P1, P7) (blue) and dropsonde (P3) (green).

References

Steven J Abel, Ian A Boutle, Kirk Waite, Stuart Fox, Philip RA Brown, Richard Cotton, Gary Lloyd, Tom W Choularton, and Keith N Bower. The role of precipitation in controlling the transition from stratocumulus to cumulus clouds in a Northern Hemisphere cold-air outbreak. *Journal of the Atmospheric Sciences*, 74(7):2293–2314, 2017. doi: 10.1175/JAS-D-16-0362.1.

Burghard Brümmer. Boundary-layer modification in wintertime cold-air outbreaks from the Arctic sea ice. *Boundary-Layer Meteorology*, 80:109–125, 1996. doi: 10.1007/BF00119014.

Burghard Brümmer, Birgit Rump, and Gottfried Kruspe. A cold air outbreak near Spitsbergen in springtime—Boundary-layer modification and cloud development. *Boundary-layer meteorology*, 61:13–46, 1992. doi: 10.1007/BF02033993.

Sandro Dahlke, Amélie Solbès, and Marion Maturilli. Cold air outbreaks in Fram Strait: Climatology, trends, and observations during an extreme season in 2020. *Journal of Geophysical Research: Atmospheres*, 127(3):e2021JD035741, 2022. doi: 10.1029/2021JD035741.

Ethan R Dale, Marwan Katurji, Adrian J McDonald, Paul Voss, Wolfgang Rack, and Daisuke Seto. A comparison of AMPS forecasts near the Ross Sea polynya with Controlled Meteorological balloon observations. *Journal of Geophysical Research: Atmospheres*, 125(20):e2019JD030591, 2020. doi: 10.1029/2019JD030591.

DLR. Dramatic warming in the Arctic. News article from German Aerospace Center. Online; [accessed May 31, 2023], 2022. URL https://www.dlr.de/en/latest/news/2022/01/20220318_halo-ac-3-field-campaign-investigates-a-worrying-phenomenon.

Dieter Etling and Robert A Brown. Roll vortices in the planetary boundary layer: A review. *Boundary-Layer Meteorology*, 65:215–248, 1993. doi: 10.1007/BF00705527.

Tony Finch. Incremental calculation of weighted mean and variance. *University of Cambridge*, 4(11-5):41–42, 2009.

Lars R Hole, Alexis Pérez Bello, Tjarda J Roberts, Paul B Voss, and Timo Vihma. Measurements by controlled meteorological balloons in coastal areas of Antarctica. *Antarctic Science*, 28(5):387–394, 2016. doi: 10.1017/S0954102016000213.

Aina Johannesen. Weathervis flexible visualization tool. Github; [accessed May 28, 2023], 2021. URL https://github.com/ainajoh/weathervis.

Marvin Kähnert, Harald Sodemann, Wim C de Rooy, and Teresa M Valkonen. On the utility of individual tendency output: revealing interactions between parameterized processes during a marine cold air outbreak. *Weather and forecasting*, 36(6):1985–2000, 2021. doi: 10.1175/WAF-D-21-0014.1.

Erik W Kolstad. A global climatology of favourable conditions for polar lows. *Quarterly*

Journal of the Royal Meteorological Society, 137(660):1749–1761, 2011. doi: doi.org/10.1002/qj.888.

Erik W Kolstad. Higher ocean wind speeds during marine cold air outbreaks. *Quarterly Journal of the Royal Meteorological Society*, 143(706):2084–2092, 2017. doi: 10.1002/qj.3068.

Anniken Celine Mentzoni. FLEXPART validation with the use of CMET balloons. Master's thesis, 2011. URL `https://www.duo.uio.no/handle/10852/12550`. [Online; accessed May 31, 2023].

Malte Müller, Yurii Batrak, Jørn Kristiansen, Morten AØ Køltzow, Gunnar Noer, and Anton Korosov. Characteristics of a convective-scale weather forecasting system for the European Arctic. *Monthly Weather Review*, 145(12):4771–4787, 2017a. doi: 10.1175/MWR-D-17-0194.1.

Malte Müller, Mariken Homleid, Karl-Ivar Ivarsson, Morten AØ Køltzow, Magnus Lindskog, Knut Helge Midtbø, Ulf Andrae, Trygve Aspelien, Lars Berggren, Dag Bjørge, et al. AROME-MetCoOp: A Nordic convective-scale operational weather prediction model. *Weather and Forecasting*, 32(2):609–627, 2017b. doi: 10.1175/WAF-D-16-0099.1.

Lukas Papritz. Synoptic environments and characteristics of cold air outbreaks in the Irminger Sea. *International Journal of Climatology*, 37:193–207, 2017. doi: 10.1002/joc.4991.

Lukas Papritz and Harald Sodemann. Characterizing the local and intense water cycle during a cold air outbreak in the Nordic seas. *Monthly Weather Review*, 146(11):3567–3588, 2018. doi: 10.1175/MWR-D-18-0172.1.

Lukas Papritz and Thomas Spengler. A Lagrangian climatology of wintertime cold air outbreaks in the Irminger and Nordic Seas and their role in shaping air- sea heat fluxes. *Journal of Climate*, 30(8):2717–2737, 2017. doi: 10.1175/JCLI-D-16-0605.s1.

Lukas Papritz, Stephan Pfahl, Harald Sodemann, and Heini Wernli. A climatology of cold air outbreaks and their impact on air–sea heat fluxes in the high-latitude South Pacific. *Journal of Climate*, 28(1):342–364, 2015. doi: 10.1175/JCLI-D-14-00482.1.

Ignacio Pisso, Espen Sollum, Henrik Grythe, Nina I Kristiansen, Massimo Cassiani, Sabine Eckhardt, Delia Arnold, Don Morton, Rona L Thompson, Christine D Groot Zwaaftink, et al. The Lagrangian particle dispersion model FLEXPART version 10.4. *Geoscientific Model Development*, 12(12):4955–4997, 2019. doi: 10.5194/gmd-12-4955-2019.

Felix Pithan, Gunilla Svensson, Rodrigo Caballero, Dmitry Chechin, Timothy W Cronin, Annica ML Ekman, Roel Neggers, Matthew D Shupe, Amy Solomon, Michael Tjernström, et al. Role of air-mass transformations in exchange between the Arctic and mid-latitudes. *Nature Geoscience*, 11(11):805–812, 2018. doi: 10.1038/s41561-018-0234-1.

Emily E Riddle, Paul B Voss, Andreas Stohl, Daniel Holcomb, Darren Maczka, K Washburn, and Robert W Talbot. Trajectory model validation using newly developed altitude-controlled balloons during the International Consortium for Atmospheric Research on Transport and Transformations 2004 campaign. *Journal of Geophysical Research: Atmospheres*, 111(D23), 2006. doi: 10.1029/2006JD007456.

Tjarda J Roberts, Marina Dütsch, Lars R Hole, and Paul B Voss. Controlled meteorological (CMET) free balloon profiling of the Arctic atmospheric boundary layer around Spitsbergen compared to ERA-Interim and Arctic System Reanalyses. *Atmospheric Chemistry and Physics*, 16(19):12383–12396, 2016. doi: 10.5194/acp-16-12383-2016.

Aurora Stenmark, Lars Robert Hole, Paul Voss, Joachim Reuder, and Marius O Jonassen. The influence of nunataks on atmospheric boundary layer convection during summer in Dronning Maud Land, Antarctica. *Journal of Geophysical Research: Atmospheres*, 119(11):6537–6548, 2014. doi: 10.1002/2013JD021287.

Andreas Stohl, C Forster, A Frank, P Seibert, and G Wotawa. The Lagrangian particle dispersion model FLEXPART version 6.2. *Atmospheric Chemistry and Physics*, 5(9): 2461–2474, 2005. doi: 10.5194/acp-5-2461-2005.

Annick Terpstra and Shun-ichi Watanabe. Polar Lows. In *Oxford research encyclopedia of climate science*. 2020. URL https://oxfordre.com/climatescience/display/10.1093/acrefore/9780190228620.001.0001/acrefore-9780190228620-e-775.

Annick Terpstra, Clio Michel, and Thomas Spengler. Forward and reverse shear environments during polar low genesis over the Northeast Atlantic. *Monthly Weather Review*, 144(4):1341–1354, 2016. doi: 10.1175/MWR-D-15-0314.1.

Richard E Thomson and William J Emery. *Data analysis methods in physical oceanography*. Newnes, 2014.

C Veness. Calculate distance and bearing between two latitude/longitude points using haversine formula in javascript. retrieved may 8, 2023, 2019. URL https://www.movable-type.co.uk/scripts/latlong.html.

Bert Verreyken, Jérome Brioude, and Stéphanie Evan. Development of turbulent scheme in the FLEXPART-AROME v1. 2.1 Lagrangian particle dispersion model. *Geoscientific Model Development*, 12(10):4245–4259, 2019. doi: 10.5194/gmd-12-4245-2019.

Timo Vihma, Roberta Pirazzini, Ilker Fer, Ian A Renfrew, Joseph Sedlar, Michael Tjernström, Christof Lüpkes, T Nygård, Dirk Notz, Jerome Weiss, et al. Advances in understanding and parameterization of small-scale physical processes in the marine Arctic climate system: a review. *Atmospheric Chemistry and Physics*, 14(17):9403–9450, 2014. doi: 10.5194/acp-14-9403-2014.

Paul B Voss, Lars R Hole, Elizabeth F Helbling, and Tjarda J Roberts. Continuous in-situ soundings in the Arctic boundary layer: A new atmospheric measurement technique using controlled meteorological balloons. *Journal of Intelligent & Robotic Systems*, 70:609–617, 2013. doi: 10.1007/s10846-012-9758-6.

John M Wallace and Peter V Hobbs. *Atmospheric science: an introductory survey*, volume 92. Elsevier, 2006.

Thomas Tomkins Warner. *Numerical Weather and Climate Prediction*. Cambridge University Press, 2010. doi: 10.1017/CBO9780511763243.